

The age-metallicity dependence for white dwarfs stars

A. D. Romero^{1*}, F. Campos¹ and S. O. Kepler¹

¹*Departamento de Astronomia, Universidade Federal do Rio Grande do Sul, Av. Bento Goncalves 9500 Porto Alegre 91501-970, RS, Brazil*

ABSTRACT

We present a theoretical study on the metallicity dependence of the initial–to–final mass relation and its influence on white dwarf age determinations. We compute a grid of evolutionary sequences from the main sequence to ~ 3000 K on the white dwarf cooling curve, passing through all intermediate stages. During the thermally-pulsing asymptotic giant branch no third dredge-up episodes are considered and thus the photospheric C/O ratio is below unity for sequences with metallicities larger than $Z = 0.0001$. We consider initial metallicities from $Z = 0.0001$ to $Z = 0.04$, accounting for stellar populations in the galactic disk and halo, with initial masses below $\sim 3M_{\odot}$. We found a clear dependence of the shape of the initial–to–final mass relation with the progenitor metallicity, where metal rich progenitors result in less massive white dwarf remnants, due to an enhancement of the mass loss rates associated to high metallicity values. By comparing our theoretical computations with semi empirical data from globular and old open clusters, we found that the observed intrinsic mass spread can be accounted for by a set of initial–to–final mass relations characterized by different metallicity values. Also, we confirm that the lifetime spent before the white dwarf stage increases with metallicity. Finally, we estimate the mean mass at the top of the white dwarf cooling curve for three globular clusters NGC 6397, M4 and 47 Tuc, around $0.53M_{\odot}$, characteristic of old stellar populations. However, we found different values for the progenitor mass, lower for the metal poor cluster, NGC 6397, and larger for the younger and metal rich cluster 47 Tuc, as expected from the metallicity dependence of the initial–to–final mass relation.

Key words: initial final mass relation – stars: evolution – metallicity – white dwarfs

1 INTRODUCTION

White dwarf stars are the most common stellar evolutionary endpoint. All stars with initial masses up to $\sim 10.5M_{\odot}$ (Smartt 2009, Doherty et al. 2014), more than 97% of the stars in the Galaxy, end their lives as white dwarf stars. Their evolution can be described as a simple and slow cooling process. Because white dwarf stars are abundant and long-lived objects they convey important information about the properties of all galactic populations (Isern et al. 2001; Liebert et al. 2005; Bono et al. 2013). In particular, white dwarf stars can be considered as reliable cosmic clocks to infer the age of a wide variety of stellar populations, such as the Galactic disks and halo (Winget et al. 1987; García-Berro et al. 1988ab, Isern et al. 1998; Torres et al. 2002), and globular and open clusters (Kalirai et al. 2001; Hansen et al. 2002, 2007; Kalirai 2013).

Methods for determining stellar population ages from their white dwarf cooling sequences are usually based on the comparison of either the observed white dwarf luminosity function (Winget et al. 1987, Bedin et al. 2010, García-Berro et al. 2014), or the distribution in the Color–Magnitude Diagram, with theoretical computations (see e.g. Hansen et al. 2007). Both techniques rely on the use of extensive grids of white dwarf cooling sequences. However, the evolutionary stages prior to the final cooling curve must be taken into account. In particular, a connection between the properties of the white dwarfs with those of their main sequence progenitors is the initial-to-final mass relation (IFMR). This relation can be applied to study the chemical evolution of galaxies, including the enrichment of the interstellar medium, and the chemical evolution history of stellar populations in general. At the high mass end, the white dwarf IFMR can lead to constraints on the critical mass that separates white dwarf production from Type II supernova explosions, and at the low mass end, the relation represents a tool to probe the pro-

* E-mail: alejandra.romero@ufrgs.br

genitor properties of most of the evolved stars in old stellar populations, the majority of which are now low-mass white dwarf stars.

The study of the IFMR started with the work of Weidemann (1977) who compared theoretical models of mass loss to the observed masses of a few white dwarfs in nearby stellar clusters. This semi-empirical approach was followed by other authors. More recently, Catalán et al. (2008a) obtained a semi-empirical IFMR by re-evaluating the available data, that includes observations from individual stars from open clusters and common proper motion pairs. Kalirai et al. (2008) increased the observations and included data from two open clusters older than ~ 1 Gyr and from the old open cluster NGC 6791, extending the initial mass range down to $1.16M_{\odot}$. Finally, Kalirai (2013) presented an IFMR based on spectroscopic observations of white dwarfs belonging to open and globular clusters and Sirius B (see e.g. Kalirai et al. 2007, 2008, 2009), with initial mass ranging from $0.8M_{\odot}$ to $\sim 6M_{\odot}$. In particular, Kalirai et al. (2008) bin the relation so that each star cluster was represented by a single point.

In the last few years, the amount of data available has increased considerably. In the Galactic field, the Sloan Digital Sky Survey increased the total number of spectroscopically confirmed white dwarfs stars to $\sim 30\,000$ (Kleinmann et al. 2013, Kepler et al. 2014). In the Galactic Halo, recent Hubble Space Telescope observations of the globular clusters M4 (Richer et al. 2004; Hansen et al. 2004; Bedin et al. 2009), ω Cen (Monelli et al. 2005), NGC 6397 (Richer et al. 2006; Hansen et al. 2007) and 47 Tuc (Hansen et al. 2013) have similarly uncovered several hundreds of cluster white dwarfs. In all cases, the white dwarf samples are dominated by low mass stars. With the increase of the available data, the general trend in the empirical IFMR remains. However, the scatter in the data has increased, possibly due to a correlation between the mass loss rates and the properties of the host environment. Although this scatter could be related to other properties as rotation, binary evolution and the presence of magnetic fields (Weidemann 2000), it is more likely produced by differences in the chemical composition, i.e. different metallicity values (Kalirai et al. 2008).

To estimate the age of a given stellar population, the metallicity of the environment has to be taken into account. As it is well known, for a fixed initial mass, the lifetime of a star decreases with the metallicity, since less metallic – lower opacity – envelopes leads to higher luminosities. On the other hand, an increase on metallicity leads to an enhanced mass loss during the giant phases of the evolution, resulting in lower final masses. In addition, other parameter characterizing white dwarf stars are expected to depend on metallicity. For instance, the amount of hydrogen left on a white dwarf star decreases for higher metallicity values (see e.g. Renedo et al. 2010). Also, a reduction of the initial metallicity tends to reduce the degree of chemical stratification in the central regions, which translates in a lower oxygen abundance at the center (Dominguez et al. 1999). This will affect the cooling rates, and in particular, the amount of energy released by the crystallization process at $T_{\text{eff}} \lesssim 12\,000$ K.

In this work we focus on the study of the effects of dif-

ferent metallicity values on the IFMR and on the lifetimes during the cooling sequences and its previous evolutionary stages. Specifically we center our analysis on the low and intermediate mass end of the IFMR, by considering masses ranging from $\sim 0.8M_{\odot}$ to $\sim 3M_{\odot}$ at the main sequence. To this end we compute full evolutionary sequences from the zero age main sequence (ZAMS), through the central stable hydrogen and helium central burning, the thermally pulsing and mass-loss phases on the asymptotic giant branch (AGB), and finally to the white dwarf cooling phase. The computations were performed with the LPCODE evolutionary code (Althaus et al. 2005a). We consider 7 metallicity values ranging from $Z = 0.0001$ to $Z = 0.04$, covering the values for halo and disk populations.

This paper is organized as follows. Section 2 is devoted to present the input physics considered in the evolutionary computations. In section 3 we present our model grid and discuss the influence of metallicity on the pre-white dwarf evolution. We explore the influence of metallicity on the minimum mass to reach helium burning at the beginning of the horizontal branch phase and the core mass growth during the TP-AGB phase. In section 4 we present and discuss our results for the theoretical IFMR for the different metallicity values and compare them with the observational data from open and globular clusters. Also, we compare our results with other theoretical and semi-empirical determinations of the IFMR. In section 5 we analyze the influence of the metallicity on structural parameters of the resulting white dwarf models, such as the amount of hydrogen and the chemical composition of the core. Section 6 is devoted to assess the effect of metallicity on the age determination of stellar populations. In particular we use our theoretical evolutionary sequences to study three well known globular cluster, NGC 6397, M4 and 47 Tuc. For this systems we estimate the mass range at the cooling sequence. We present our concluding remarks in section 7.

2 NUMERICAL TOOLS

The evolutionary computations presented in this work were calculated with an updated version of the LPCODE evolutionary code. The details on the code can be found in Althaus et al. (2005a, 2010), Renedo et al. (2010) and Romero et al. (2013). The LPCODE evolutionary code computes the complete evolution from the ZAMS, through the hydrogen and helium burning stages, the thermally pulsating and mass loss stages on the asymptotic giant branch, to the white dwarf cooling evolution. This code has been used to produce very accurate white dwarf models (see García-Berro et al. 2010; Althaus et al. 2010; Renedo et al. 2010 and reference therein). The code has also been used to study the formation of extreme horizontal branch stars (Miller Bertolami et al. 2008), the evolution of extremely low mass white dwarf stars (Althaus et al. 2013), and also the role of thermohaline mixing for the surface composition of low-mass red giants (Wachlin et al. 2011).

2.1 Pre-white dwarf evolution

The LPCODE considers simultaneous treatment of non-instantaneous mixing and burning of elements (Althaus et al. 2003). The nuclear network accounts for 16 elements and 34 reaction rates, that includes *pp*-chain, CNO-cycle, helium burning and carbon ignition (Althaus et al. 2005b). Reaction rates are taken from Caughlan & Fowler (1988) and Angulo et al. (1999). In particular, the $^{12}\text{C}(\alpha, \gamma)^{16}\text{O}$ reaction rate, of special relevance for the carbon-oxygen stratification of the resulting white dwarf, was taken from Angulo et al. (1999). The radiative opacities are those of the OPAL project (Iglesias & Rogers 1996), including carbon- and oxygen-rich compositions, supplemented at low temperatures with the molecular opacities of Ferguson et al. (2005) and Weiss & Ferguson (2009). In LPCODE molecular opacities are computed adopting the opacity tables with the correct abundances of the unenhanced metals and the appropriate carbon-oxygen ratio. For the present computations, we have not considered carbon-enriched molecular opacities (Marigo 2002), which are expected to reduce effective temperatures at the AGB (Wiess & Ferguson 2009). Conductive opacities are those from Cassisi et al. (2007). Neutrino emission rates for pair, photo and bremsstrahlung processes are taken from Itoh et al. (1996), and for plasma processes the treatment of Haft et al. (1994) is included. We adopted the standard mixing length theory with the free parameter $\alpha = 1.6$. With this value, the present luminosity and effective temperature of the Sun, $\log T_{\text{eff}} = 3.7641$ and $L_{\odot} = 3.842 \times 10^{33} \text{ erg s}^{-1}$ at an age of 4570 Myrs, are reproduced by LPCODE when $Z = 0.0164$ and $X = 0.714$ are adopted, in agreement with the Z/X value of Grevesse & Sauval (1998), which are better reproduced by helioseismology than more recent determinations (Basu & Antia 2008).

During the evolutionary stages prior to the thermally pulsing AGB phase, we allow the occurrence of extra-mixing episodes beyond each convective boundary following the prescription of Herwig et al. (1997). Note that the occurrence of extra-mixing episodes during the core helium burning phase largely determines the final chemical composition of the core of the resulting white dwarf star (Prada Moroni & Straniero 2002, Straniero et al. 2003). We treated the extra-mixing as a time-dependent diffusion process, assuming that the mixing velocities decay exponentially beyond each convective boundary. The diffusion coefficient is given by $D_{\text{EM}} = D_0 \exp(-2z/fH_P)$, where H_P is the pressure scale height at the convective boundary, D_0 is the diffusion coefficient of unstable regions close to the convective boundary, and z is the geometric distance from the edge of the convective boundary (Herwig et al. 1997, 2000). The free parameter f describes the efficiency of the extra-mixing process. It can take values as high as $f \sim 1.0$, for over-adiabatic convective envelopes of DA white dwarfs (Freytag et al. 1996). However, for deep envelope and core convection f is expected to be considerably smaller because the ratio of the Brunt-Väisälä timescales of the stable to unstable layers decreases with depth. We assume $f = 0.016$, which accounts for the location of the upper envelope on the main sequence for a large sample of clusters and associations (Schaller et al. 1992, Herwig et al. 1997, 2000). The same value accounts for the intershell abundances of

hydrogen-deficient post-AGB remnants (see Herwig et al. 1997; Herwig 2000; Mazzitelli et al. 1999). Finally, for the mass range considered in this work, the mass of the outer convection zone on the tip of the RGB only increases by $\sim 1.5\%$ if we change the parameter f by a factor of two. The breathing pulse instability occurring towards the end of the core helium burning is attributed to the adopted algorithm rather than to the physics of convection and therefore were suppressed in our computations (see Straniero et al. 2003 for a detailed discussion).

During the thermally pulsing AGB phase, extra-mixing episodes were disregarded. This may prevent the third dredge-up to occur in low mass stars. In particular, a strong reduction of extra-mixing episodes at the base of the pulse-driven convection zone seems to be supported by simulations of the *s*-process abundance patterns (Lugaro et al. 2003) and by observational inferences of the IFMR (Salaris et al. 2009). As a consequence, we expect that the mass of the hydrogen free core to gradually increase as evolution proceeds during this stage. Kalirai et al. (2014) estimated a growth of the core mass on the TP-AGB to be between 10% and 30% for initial masses between $1.6M_{\odot}$ and $2.0M_{\odot}$, that decreases steadily to $\sim 10\%$ at $M_{\text{ZAMS}} = 3.4M_{\odot}$. However, third-dredge-up episodes are not completely suppressed in our models. In particular, the two more massive sequences for $Z = 0.0001$, those with initial masses 2.0 and $2.5 M_{\odot}$ do experience dredge-up episodes during the TP-AGB. We will comment on the effect of third dredge-up episodes on our determination of the final masses in section 3.3. In addition, the suppression of dredge-up episodes in our models prevents the formation of carbon rich stars, i.e, the C/O ratio remains below unity during all the TP-AGB stage.

Mass loss was considered during red giant branch and core helium burning phases following Schröder & Cuntz (2005). This mass-loss rate is based on the Reimers formula $\dot{M} = \eta L_* R_* / M_*$ (Reimers 1975), but it contains two additional factors, one depending on the surface temperature and the other on the surface gravity of the star. This improves the agreement with the observed mass-loss rates for different types of stars, without the need to adjust the fitting parameter η (Schröder & Cuntz 2005). We set $\eta = 8 \times 10^{-14} M_{\odot} \text{ yr}^{-1}$, that satisfies the well constrained RGB mass loss of globular cluster stars.

During the AGB and TP-AGB phases, we employ the prescriptions of Groenewegen et al. (2009) and Vassiliadis & Wood (1993) for low and high metallicity sequences, respectively. The mass loss prescription presented by Vassiliadis & Wood (1993) for the TP-AGB phase is pulsation dependent, with an exponentially increasing rate for periods less than ~ 500 days and a constant superwind phase for periods beyond ~ 500 days, corresponding to a radiation-pressure driven wind. This prescription, or an updated version, is usually adopted to model the mass loss during the TP-AGB stage in evolutionary computations (e.g. Renedo et al. 2010, Karakas & Lattanzio 2007, Karakas 2010, Marigo & Girardi 2007). In particular, Doherty et al. (2014) employed the mass-loss rate prescription of Vassiliadis & Wood (1993) to determine the IFMR of intermediate mass stars with initial masses between 5.0 and $10.0 M_{\odot}$ for metallicities span-

ning the range of $Z = 0.02 - 0.0001$. Groenewegen et al. (2009) presented a mass loss prescription based on data of resolved stars on the Small and Large Magellanic Clouds obtained with Spitzer IRS that represents low metallicity populations. They found that, even when the Vassiliadis & Wood (1993) models described the data better, there are some deficiencies, in particular the maximum adopted mass-loss rate. The assumption of typical velocities and dust-to-gas ratios of galactic stars may lead to an overestimate of the mass-loss rate. Therefore we employ the mass loss prescription of Groenewegen et al. (2009) for low metallicity sequences as it is better calibrated in this metallicity range. For metallicities larger than $Z = 0.01$, mass-loss rate from Groenewegen et al. (2009) are systematically lower than those from Vassiliadis & Wood (1993) and the well known superwind phase at the end of the thermally pulsing stage is rarely reached even after the star moves significantly to redder effective temperatures. For this reason we employ the prescription of Groenewegen et al. (2009) for evolutionary sequences characterized by initial metallicities $Z \leq 0.008$; and the Vassiliadis & Wood (1993) mass-loss rates for sequences with initial metallicities $Z \geq 0.01$, that better reproduce mass loss rates for high Z .

2.2 White dwarf evolution

During the white dwarf evolution, we consider the distinct physical process that modify the chemical abundances distribution. For instance, element diffusion strongly modifies the chemical composition profile throughout the outer layers. Indeed, our sequences developed a pure hydrogen envelope with increasing thickness as evolution proceeds. Our treatment of time-dependent diffusion is based on the multicomponent gas treatment presented in Burgers (1969). We consider gravitational settling and thermal and chemical diffusion of H, ^3He , ^4He , ^{12}C , ^{13}C , ^{14}N and ^{16}O (Althaus et al. 2003). To account for convection in our models we adopted the mixing length theory, in its ML2 flavor, with the free parameter $\alpha = 1$ (Tassoul et al. 1990). The metal mass fraction in the envelope is not fixed, but it is computed consistently according to the predictions of element diffusion. To account for the different envelope compositions, we considered radiative opacity tables from OPAL for arbitrary metallicities. For effective temperatures less than 10 000 K we include the effects of molecular opacity from the computations of Marigo & Aringer (2009). In addition, we considered the chemical rehomogenization of the inner carbon-oxygen profile induced by Rayleigh-Taylor instabilities following Salaris et al. (1997). For effective temperatures below 10 000 K, outer boundary conditions are derived from non-gray model atmospheres (Rohrman et al. 2012). The equation of state is that of Segretain et al. (1994) for the high density regime, which accounts for all the important contributions for both the liquid and solid phases (Althaus et al. 2007), complemented at the low-density regime with an updated version of the equation of state of Magni & Mazitelli (1979).

Finally, cool white dwarf stars are expected to undergo crystallization as a result of strong Coulomb interactions in their dense interiors (van Horn 1968). Crystallization occurs when the energy of the Coulomb interaction between neigh-

boring ions is much larger than their thermal energy. This process leads to the release of latent heat and of gravitational energy associated with changes in the chemical composition of carbon-oxygen profile (García-Berro et al. 1988ab). These additional energy sources associated with crystallization were included self-consistently, modifying the luminosity equation to account for both the local contribution of energy released from the core chemical redistribution and the latent heat, the later being of the order of $0.77k_B T$ per ion. To assess the enhancement of oxygen in the crystallized core we used the phase diagram presented in Horowitz et al. (2010) – see also Hugoto et al. (2012) and Schneider et al. (2012) –, consistent with the observations of Winget et al. (2009; 2010) of the white dwarf luminosity function of the globular cluster NGC 6397. Horowitz et al. (2010) employed molecular dynamic simulations considering liquid and solid phases in mixed composition, allowing a better determination of the melting temperature and the composition of the liquid and solid phases. They predicted an azeotropic type phase diagram, and a melting temperature lower than that predicted by Segretain & Chabrier (1993). Note that the results obtained by Horowitz et al. (2010) are in good agreement with the results of Medin & Cumming (2010), based on a semi-analytic method.

Althaus et al (2012) presented an study of the influence of the Horowitz et al. (2010) phase diagram on the evolutionary properties of white dwarf stars, specifically on the cooling times. They found that the amount of mass redistributed in the phase separation is smaller for Horowitz et al. (2010) phase diagram than for the Segretain & Chabrier (1993) one, leading to a smaller energy release from carbon-oxygen differentiation. Also, the composition changes are less sensitive to the initial chemical profile, so the cooling delay is less affected by the uncertainties in the carbon-oxygen initial abundances. Romero et al. (2013) study the effects of the two crystallization phase diagrams on the pulsation spectrum of variable DA white dwarf stars with stellar mass $\geq 0.72M_\odot$. They showed that, for a given stellar mass, computations employing the Segretain & Chabrier (1993) phase diagram was ~ 1000 K higher than that predicted by the Horowitz et al. (2010) formulation. From their asteroseismological fits they found that the phase diagram presented in Horowitz et al. (2010) is the one that better represents the crystallization process in the dense interiors of white dwarf stars.

The LPCODE has been tested against other white dwarf evolution code, and the uncertainties in the white dwarf cooling ages arising from different numerical implementations of stellar evolution equations were found to be below 2% (Salaris et al. 2013).

3 MODEL GRID AND THE PRE-WHITE DWARF EVOLUTION

3.1 Model Grid

The current grid of evolutionary models is composed by a set of sequences with initial mass between $0.8M_\odot$ and $3M_\odot$ at the ZAMS, considering also different metallicity values for the progenitor star between $Z = 0.0001$ to 0.04. Note

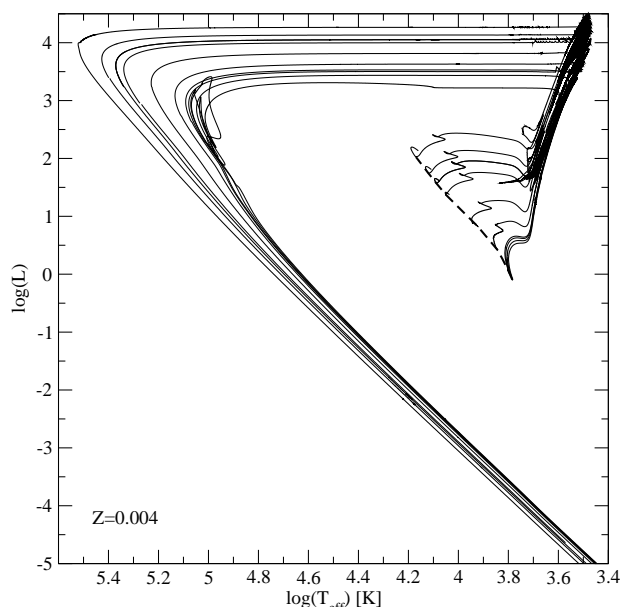


Figure 1. Hertzsprung–Russell diagram of our evolutionary sequences for $Z = 0.004$. From bottom to top: evolution of the $0.92M_{\odot}$, $0.95M_{\odot}$, $0.98M_{\odot}$, $1.0M_{\odot}$, $1.2M_{\odot}$, $1.5M_{\odot}$, $2.0M_{\odot}$, $2.25M_{\odot}$, $2.5M_{\odot}$ and $3.0M_{\odot}$ model stars. The dashed line represents the location of the Zero Age Main Sequence. Note that the sequences with an initial mass of $0.92M_{\odot}$ and $0.95M_{\odot}$ experience an hydrogen sub-flash at high effective temperatures, before entering the cooling sequence.

that in this mass range, all sequences end their lives as carbon–oxygen core white dwarf stars. The initial helium content for the starting model at the ZAMS was provided by the relation $Y = 0.245 + 2Z$, where Z represents the initial metallicity. Our results are summarized in Table 1, where we list the initial and final masses for all metallicity values considered in this work. For each sequence we also list the progenitor age, i.e., the age from the ZAMS to the point of maximum effective temperature before entering the white dwarf cooling curve (t_{prog}). The sequences with $Z = 0.01$ and $Z = 0.001$, except for the sequences with initial mass of 0.92 and $1.1M_{\odot}$ for the latter Z , are based on those from Renedo et al. (2010). Since these authors employ the Segre-tain et al. (1993) formulation of the phase diagram for crystallization, we recalculated the final evolution of the white dwarf cooling considering the Horowitz et al. (2010) prescription. The remaining sequences were computed specifically for this work. Additional sequences characterized by high and very low metallicity values, those with $Z = 0.05$ and $Z = 0.00001$, were computed to assess the dependence of the final mass with metallicity, but also of other parameters as the amount of mass lost and the size of the helium core at the beginning of the central helium burning stage (see section 3.2).

The evolution in the Hertzsprung–Russell diagram from the ZAMS to advanced stages of white dwarf evolution for $Z = 0.004$ is shown in Figure 1 for sequences with initial masses larger than $0.90M_{\odot}$. Typically, sequence with initial mass lower than $\sim 0.95M_{\odot}$ experience an hydrogen sub-flash before entering its final cooling track. Hydrogen sub-flashes

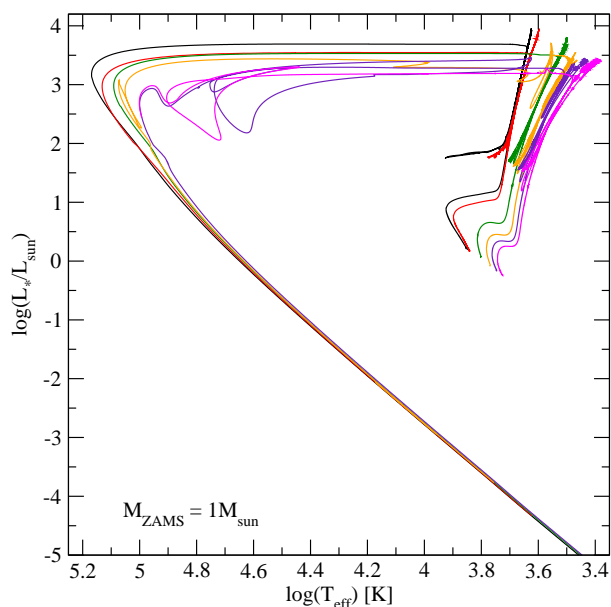


Figure 2. Hertzsprung–Russell diagram of our evolutionary sequences with initial stellar mass of $1M_{\odot}$ with metallicities of $Z = 0.00001, 0.0001, 0.004, 0.01, 0.02$ and 0.04 from top to bottom.

are a consequence of an increase in the luminosity due to shell hydrogen burning at high effective temperatures during the evolution towards the white dwarf cooling curve. For $Z = 0.004$ the hydrogen sub-flashes are present for sequences with 0.9 and $0.92M_{\odot}$. In addition, sequences characterized by the lowest initial stellar mass on the ZAMS usually do not go through the AGB and thermally pulsing AGB stages ($0.90M_{\odot}$ for $Z = 0.004$). These sequences spend the core helium burning stage at the blue edge of the Horizontal Branch phase and move directly to the white dwarf cooling curve without experiencing the high luminosity phase.

In Fig. 2 we show the evolutionary sequences characterized by a $1M_{\odot}$ at the ZAMS and different initial metallicity values. When metallicity increases, the position of the main sequences moves towards lower luminosities and effective temperatures, since the atmospheres of more metallic stars are more opaque, and then the larger opacities make the models move towards redder temperatures. On the other hand less metallic models are more luminous because the atmospheres are more transparent. This is also true when we inspect the AGB and TP-AGB stages; less metallic models are dislocated to the blue because of the lower opacities. As we mention in section 2.1 the mass-loss rate is metallicity dependent (Vasiliadis & Wood 1993; Groenewegen et al. 2009), then the less metallic sequences have less efficient mass loss episodes, leading to a larger number of thermal pulses.

In the present work, the hydrogen content of the sequences correspond to the value predicted by standard stellar evolution and should be considered as upper limits for the maximum hydrogen content left in the white dwarf resulting for the evolution of single star progenitors. As we will show in section 5.1, the amount of hydrogen left on a white dwarf envelope depends on stellar mass and metallicity (see

Table 1. Initial and final stellar masses (in solar units) and progenitor ages (in Gyr) for the metallicity values considered in Figure 4. Values corresponding to $Z=0.01$ and most to $Z=0.001$ are extracted from Renedo et al. (2010) (see text for details).

M_{ZAMS}	$Z = 0.0001$		$Z = 0.001$		$Z = 0.004$		$Z = 0.008$		$Z = 0.01$		$Z = 0.02$		$Z = 0.04$	
	M_{WD}	t_{prog}	M_{WD}	t_{prog}	M_{WD}	t_{prog}	M_{WD}	t_{prog}	M_{WD}	t_{prog}	M_{WD}	t_{prog}	M_{WD}	t_{prog}
0.80	0.519	12.742
0.85	0.534	10.327	0.505	13.322
0.90	0.550	8.421	0.503	11.898	0.489	15.767
0.92	0.536	9.789	0.515	10.978
0.94	0.508	13.037
0.95	0.561	6.998	0.524	9.772	0.493	13.350	0.488	15.160
0.98	0.533	8.736	0.516	11.679
1.00	0.569	5.871	0.553	7.442	0.537	8.076	0.524	10.788	0.525	11.117	0.511	12.512	0.511	13.327
1.05	0.531	8.053
1.10	0.566	5.274	0.547	5.800	0.538	7.339
1.20	0.553	4.310	0.552	5.047
1.25	0.621	2.826	0.593	3.449
1.50	0.669	1.593	0.627	1.897	0.599	2.080	0.588	2.382	0.570	2.700
1.75	0.708	1.038	0.660	1.324	0.593	1.699
2.00	0.737	0.752	0.693	0.947	0.665	1.074	0.638	1.074	0.609	1.211	0.591	1.286	0.566	1.368
2.25	0.691	0.788	0.632	0.989
2.50	0.826	0.423	0.730	0.579	0.660	0.742
3.00	0.875	0.274	0.864	0.326	0.817	0.352	0.705	0.443	0.656*	0.461

*Mass of the degenerate core at the last thermal pulse.

e.g. Renedo et al. 2010, Romero et al. 2012). The amount of hydrogen left in a white dwarf star is an important factor to determine the cooling ages, since hydrogen has a larger opacity than helium. Cooling ages can be reduced by 10% for thin hydrogen envelopes ($10^{-10}M_*$) at $\log(L/L_\odot) = -5.5$ (Catalán et al. 2008a) in comparison with thick ones. In addition, a thinner hydrogen envelope can be mixed with the underlying helium layer when the outer convective zone at the white dwarf atmosphere reaches the hydrogen-helium interface at low effective temperatures, turning the hydrogen atmosphere star into a helium atmosphere white dwarf (Tremblay & Bergeron 2008; Romero et al. 2013; Kurtz et al. 2013). Evidence from asteroseismology (Castanheira & Kepler 2009; Romero et al. 2012, 2013) showed that the mass of the hydrogen layer spreads over $10^{-4} - 10^{-10}M_*$ with a mean value around $10^{-6}M_*$, two orders of magnitude smaller than the white dwarf models in the literature employed in evolutionary studies of this type of star.

3.2 The core mass at helium ignition

In this section we analyze the impact of metallicity on the mass of the helium core at the beginning of the central helium burning stage, and also on the total mass lost in the different giant phases. In Table 2 we list the final mass values along with some other relevant parameters for all sequences with initial mass of $1M_\odot$ and $2M_\odot$. We computed additional sequences, apart from those listed in Table 1 with $Z = 0.00001$, $Z = 0.03$ and $Z = 0.05$ for $M_{\text{ZAMS}} = 1M_\odot$, and $Z = 0.03$ for $M_{\text{ZAMS}} = 2M_\odot$. The second column of Table 2 lists the mass of the helium core before the onset of helium burning, i.e., the hydrogen free core mass at the end of the RGB phase. For all sequences with a $1M_\odot$ progenitor and the sequences with a progenitor star with $2M_\odot$

and metallicity $Z \geq 0.01$, this mass is the mass of the helium core at the maximum of the helium luminosity during the helium flash. Note that for sequences with initial mass $1M_\odot$, the mass of the helium core increases with decreasing metallicity approximately $0.052M_\odot$ in the range considered in this work. This can be seen also from Fig. 3 where we plot the mass of the helium core at the beginning of the central helium burning stage as a function of metallicity for sequences with initial stellar mass of $1M_\odot$ (squares) and $2M_\odot$ (circles).

For sequences with progenitor mass of $2M_\odot$ we have two groups, those sequences with initial metallicity below $Z = 0.01$ do not experience an helium ignition on a degenerate core. As a consequence the mass of the helium core at the beginning of the central helium burning is significantly lower, around $0.32 - 0.33M_\odot$. On the other hand, sequences with initial metallicities ranging from 0.01 to 0.04 ignite the central helium in a degenerate state. Although the mass of the helium core at this point is lower than that for the $1M_\odot$ sequences, it is higher compared to the metal poor cases. This change in the central helium core mass is clear in Fig. 3. In particular, we note that the helium core mass is maximum for $Z = 0.02$ and then decreases for lower and higher metallicities. Also, the maximum helium luminosity at the moment of the helium flash is 3-4 orders of magnitude larger for the sequences with $Z = 0.02$. From stellar evolutionary theory we know that the size of the final hydrogen free core is mainly controlled by two processes: mass-loss and overshooting. Mass-loss rates decreases with decreasing metallicity, allowing the core to increase its size given the larger amount of burning material. On the other hand, even though mass-loss rates increases with metallicity, the influence of overshooting is more important for high Z , also allowing the core to increase its size. For Z as high

Table 2. Different parameters as a function of the metallicity of the progenitor star with initial mass $1M_{\odot}$ (squares) and $2M_{\odot}$ (circles) at the ZAMS. The columns list the metallicity value, the mass of the hydrogen free core at the helium flash or at the beginning of the helium central burning stage, the mass lost during the Red Giant Branch and Asymptotic Giant Branch phases and the final mass at the white dwarf cooling sequence. All masses are in solar units.

Z	$M_{\text{ZAMS}} = 1M_{\odot}$				$M_{\text{ZAMS}} = 2M_{\odot}$			
	M_{HFC}	$\Delta M(\text{RGB})$	$\Delta M(\text{AGB})$	M_{WD}	M_{HFC}	$\Delta M(\text{RGB})$	$\Delta M(\text{AGB})$	M_{WD}
0.00001	0.5066	0.1068	0.3280	0.564
0.0001	0.4986	0.1374	0.2960	0.562	0.3263	0.0001	1.2006	0.738
0.001	0.4855	0.1782	0.2535	0.553	0.3227	0.0021	1.2725	0.693
0.004	0.4807	0.2342	0.2168	0.537	0.3185	0.0023	1.3195	0.665
0.008	0.4789	0.2834	0.1818	0.524	0.3225	0.0028	1.3492	0.638
0.01	0.4789	0.3218	0.1410	0.525	0.4047	0.0172	1.3565	0.609
0.02	0.4705	0.3628	0.1169	0.511	0.4172	0.0243	1.3777	0.591
0.03	0.4661	0.3870	0.0883	0.511
0.04	0.4596	0.3912	0.0887	0.511	0.3910	0.0149	1.4126	0.566
0.05	0.4547	0.3747	0.1004	0.515

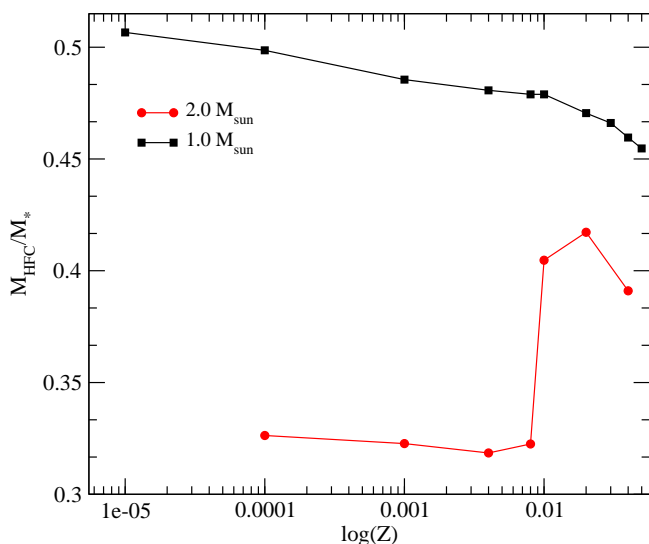


Figure 3. Mass of the hydrogen free core at the beginning of the central helium burning stage as a function of metallicity, for sequences with $1M_{\odot}$ (squares) and $2M_{\odot}$ (circles) at the ZAMS. Note that the larger the mass at the ZAMS, the smaller the mass of the hydrogen free core.

as 0.05 the overshooting influence could be overcoming the influence of mass loss.

Also listed in Table 2 are the total mass lost during the RGB and AGB phases. For the sequences with a progenitor star of $1M_{\odot}$ we see that the mass lost during the RGB increases with increasing metallicity, leaving a smaller amount of mass to be lost during the AGB phase. In fact, sequences with the highest values of Z do not experience any thermal pulses and the growth in the carbon–oxygen core is only due to the evolution during the AGB. On the other hand, the low metallicity sequences experience up to 4–5 thermal pulses, extending their stay at the high luminosity stage. For the sequences with a progenitor star of $2M_{\odot}$ the mass lost during the RGB is negligible compared with the total mass lost during the AGB and thermal pulsing AGB. Practically

all mass is lost during the late stages of the evolution. Because of this, the modeling of the mass–loss rates becomes so important during the AGB and TP-AGB.

Finally, the dependence of the final mass with the progenitor metallicity also has an impact on the inner composition of a given white dwarf star. Since the final mass is higher for lower metallicities, low mass carbon–oxygen white dwarf can have lower mass progenitors at lower metallicity. On the other hand, for lower main sequence stars, the mass of the helium core at the helium flash increases with decreasing metallicity. For instance, a white dwarf with a stellar mass of $\sim 0.5M_{\odot}$ resulting from a $1M_{\odot}$ progenitor star could have an helium core if the initial metallicity is lower than $Z = 0.001$, but it will be a carbon–oxygen core white dwarfs for higher metallicity values, according to our single star evolution computations.

3.3 Core mass growth during the thermal pulsing AGB

After helium exhaustion in the central core, the star moves to the AGB. In the early stages, the helium burning shell increases the carbon–oxygen core mass as it moves towards the surface. In our computations, overshooting is taken into account during the early AGB, with an efficiency parameter of $f = 0.016$, while it is disregarded during the following thermal pulsing stage. A reduction of extra–mixing episodes at the base of the driving convection zone during the TP-AGB could prevent the third dredge–up to occur, specially in low mass stars. The occurrence of the third dredge–up cause an instantaneous reduction of the core mass, dragging processed material, specially carbon, to the surface (see e.g. Weiss & Ferguson 2009; Karakas et al. 2010; Marigo et al. 2013). The efficiency of the third dredge–up is usually parametrized by the parameter λ^1 , which increases with each thermal pulse until a maximum value λ_{max} (see

¹ The efficiency parameter λ is defined as the fraction of the core–mass growth over the interpulse period that is dredge–up to the surface at the next thermal pulse

e.g. Marigo et al. 2013). The value of λ_{\max} typically increases with the stellar mass, while it decreases at larger metallicities. Then, dredge-up episodes are expected to be more efficient for high masses and low metallicities. Unfortunately, the efficiency λ is one of the most uncertain parameters of TP-AGB modeling, and it is very dependent on the adopted treatment of convection, mixing, and numerical codes (Marigo et al. 2012; Kalirai et al. 2014).

Extra-mixing episodes during the TP-AGB also leads to the formation of carbon rich stars. Studies of AGB stellar populations in our Galaxy and the Magellanic Clouds shows that stars with initial mass $< 2M_{\odot}$ and low metallicity values do become carbon rich stars (Groenewegen et al. 1993; Stancliffe et al. 2005; Marigo & Girardi 2007). For instance, carbon rich stars must be formed for initial masses as low as $1M_{\odot}$ in the Large Magellanic Cloud in order to reproduce the carbon stars luminosity function (Sancliff et al. 2005). Carbon enrichment of the atmosphere will cause an abrupt change in the molecular equilibrium leading to a rise of the atmospheric opacity. This causes an increase in the mass-loss rate, leading to an early end of the TP-AGB and thus a reduction of the final mass. Because in our computations we disregarded extra-mixing episodes, our sequences in general do not experience dredge-up episodes during the TP-AGB evolution, except for the three more massive sequences, corresponding to the lowest metallicity of our grid. In our models, sequences with initial masses between $2M_{\odot}$ and $3M_{\odot}$ and $Z = 0.0001$ do experience dredge-up episodes during the TP-AGB evolution, with values of λ_{\max} of $\sim 0.22 - 0.36$, increasing with stellar mass. The mass of the core for the onset of the third dredge-up also increases from $0.652M_{\odot}$ to $0.836M_{\odot}$ for the same mass range. This values are $\sim 10 - 20\%$ larger in comparison to the results of Wiess & Ferguson (2009) for $Z = 0.0005$, adopting $f = 0.016$. Finally, all our sequences that experience dredge-up episodes become carbon-rich stars. We found that it only takes one dredge-up episode to get a carbon-rich surface, leading to a C/O ratio of $\sim 8 - 10$ at the end of the TP-AGB. This values of C/O are much higher than the C/O $\sim 1.28 - 2.0$ found in Galactic carbon stars (Lambert et al. 1986; Ohnaka et al. 2000). Note that the input physics in LPCODE is dedicated to model in detail the inner structure of the star for all evolutionary stages, and specially the white dwarf stage. However, it does not compute a detailed atmosphere model, similar to most full evolutionary codes in the literature. It is no tailored to reproduce the atmosphere abundances found in AGB stars.

To asses the effect of the extra-mixing episodes on our determinations of the final mass, we calculated additional sequences allowing extra-mixing episodes to occur, by considering different values of the overshooting parameter f . Wiess & Ferguson (2009) consider $f = 0.016$, and found that the final mass was very similar to that of the first thermal pulse, as a consequence of the enhanced dredge-up. On the other hand Lugaro et al. (2003) argued for a lower efficiency $f = 0.008$, to achieve a better agreement with detailed s -process observed abundance patterns. We computed sequences with initial mass of $2M_{\odot}$ and metallicity $Z = 0.01$ with different values of $f = 0.016, 0.008$ and 0.002 . Note that the core mass growth during the thermal pulses is

by far larger for sequences with initial masses $\sim 2M_{\odot}$, where the core mass at the first thermal pulse shows a strong minimum (Renedo et al. 2010; Marigo et al. 2013; Kalirai et al. 2014). All three sequences computed with some amount of overshooting do become carbon stars after 10 – 11 thermal pulses and ~ 4 dredge-up episodes, with C/O ratios of $\sim 1.3 - 1.5$ at the end of the TP-AGB evolution, and values of λ_{\max} from 0.63 for $f = 0.002$ to 0.94 for $f = 0.016$. Regarding the core mass growth, we found that the final mass of the hydrogen free core is reduced by 6.2%, 7.6% and 9.4% when f takes values of 0.002, 0.008 and 0.016, respectively. As a result, the final mass can be overestimated by less than 10% in our computations for this metallicity. For lower values of Z , like $Z = 0.004$ and the same initial mass, we found a larger reduction of the final mass by $\sim 15\%$, when $f = 0.008$. This is in agreement with the fact that dredge-up episodes are more efficient for lower metallicity values. Karakas et al. (2002) showed that even for low metallicity values as $Z = 0.004$, λ_{\max} is maximum for $M_{\text{initial}} \sim 2.5M_{\odot}$ and then slowly decreases for larger masses, leading to a less efficient reduction of the core mass due to dredge-up episodes. Then, in the worst case scenario, the uncertainties in final masses from our treatment of overshooting episodes might be up to $\sim 15\%$ for lower metallicities. Note that, additional uncertainties on the final core mass arise from the possible reduction of TP-AGB lifetimes when C-rich molecular opacities are considered, leading to an increase in the surface opacity and an enhanced mass-loss rate at this stage.

Finally, Kalirai et al. (2014) performed an study of the core mass growth covering the intermediate-mass range of the IFMR. They use data from four open clusters with nearly solar metallicities: NGC 6819, NGC 7789, Hyades and Praesepe, the first three included in our analysis of the initial-to-final mass relation (see section 4). As a result, they found that, in order to fit the data, the dredge-up efficiency λ_{\max} increases from zero to ~ 0.5 for initial mass from $\sim 2M_{\odot}$ to $\sim 3M_{\odot}$ and then progressively decreases for larger initial masses. From our theoretical results with $Z = 0.002$ we found a core mass growth of $\sim 10\%$ to $\sim 28\%$ for stars with initial mass $1.6M_{\odot}$ and $2.8M_{\odot}$, decreasing steadily to $\sim 6\%$ at $M_{\text{initial}} = 3.7M_{\odot}$, somewhat smaller than the results of Kalirai et al. (2014), but still in excellent agreement. In addition, Kalirai et al. (2014) found that the dominant process governing the growth of the core is largely the stellar wind, while the third dredge-up, although not negligible, plays a secondary role. They also found that the mass loss prescription that better fits the semi-empirical data is that of Vasilidis & Wood (1993), the same mass loss prescription employed in our work for solar metallicity.

4 INITIAL-TO-FINAL MASS RELATION

In this section we show our results for the theoretical IFMR and its dependence with the different metallicity. Given our model grid, we focus on the low and intermediate mass domain of the IFMR, and consider sequences with an initial mass $\leq 3M_{\odot}$. This accounts for globular clusters and old open clusters, having main sequence stars within this mass range. For young open clusters with ages of the order of ~ 100 Myr, low mass stars have no time to evolve out of

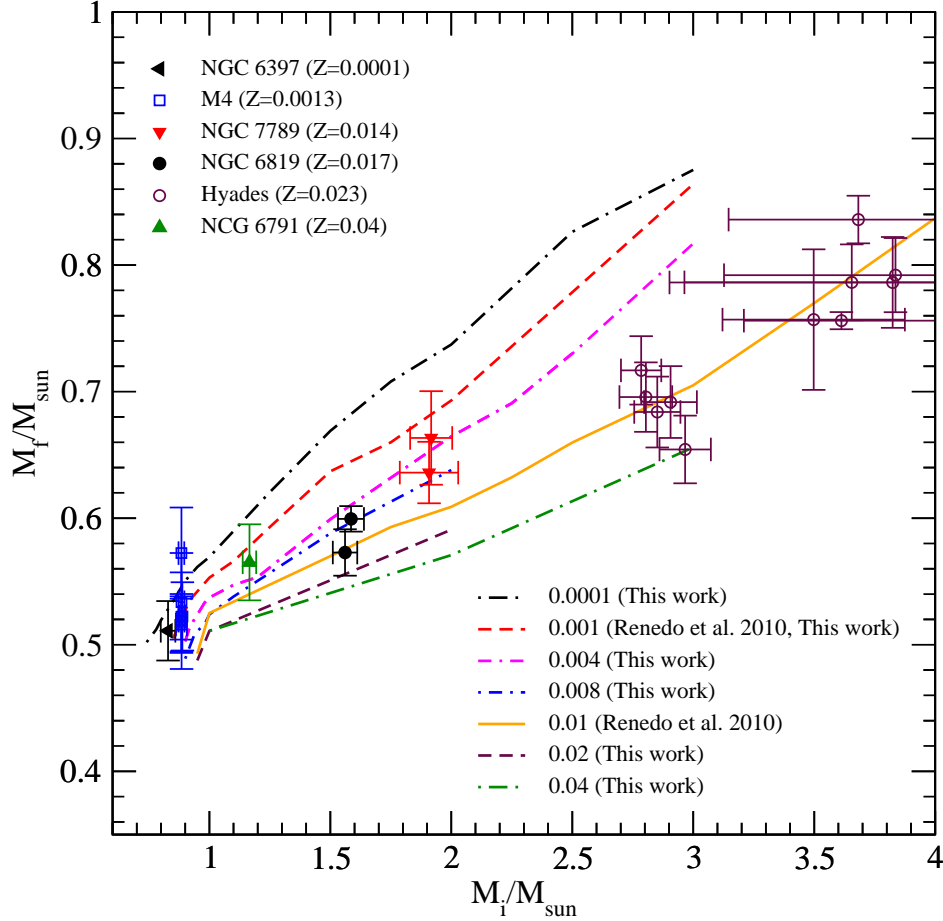


Figure 4. Theoretical IFMR for different metallicity values from $Z = 0.0001$ to $Z = 0.04$ and initial mass $\leq 3M_{\odot}$. Values for $Z = 0.01$ and initial mass larger than $3M_{\odot}$ are taken from Renedo et al. (2010). All computations were made by using the LPCODE evolutionary code. We also include some observational data for globular and old open clusters – see text for details. (A color version of this figure is available in the on-line journal.)

the main sequences yet. The initial mass (M_{ZAMS}), the final mass (M_{WD}) and the progenitor lifetime for each evolutionary sequences for all the metallicities are listed in Table 1.

We consider the final mass as that of the white dwarf star in the cooling curve, where the mass-loss rate becomes negligible, not the mass of the hydrogen free core in the first thermal pulse. As show in section 3.3 and by Kalirai et al. (2014) the mass of the hydrogen free core increases during the TP-AGB as much as 30% for $M_{initial} \sim 2.0M_{\odot}$. Then, the IFMR for a fixed metallicity by the end of the thermally pulsing AGB becomes markedly different from that determined by the mass of the hydrogen free core at the first thermal pulse (Althaus et al. 2010). For instance, if we take a white dwarf with a stellar mass of $0.63M_{\odot}$, the initial mass would be overestimated by $\sim 0.75M_{\odot}$ if we were to consider an IFMR at the first thermal-pulse, instead of the real one, at advanced stages in the thermally pulsing AGB. For the carbon-oxygen composition expected in the core of a white dwarf, this is an important issue (Althaus et al. 2010).

In Figure 4 we plot the initial-to-final mass relation. Each curve represents a set of theoretical computations with a given initial metallicity value. From this figure we can see

that the IFMR shows a dependence with metallicity: for a given initial mass of the progenitor star, the mass of the resulting white dwarf remnant decreases when metallicity increases. This effect is noticeable for progenitor mass above $\sim 1M_{\odot}$. For instance, the mass of the resulting white dwarf evolving from a $2M_{\odot}$ progenitor star is $\sim 21\%$ larger when the metallicity decreases from $Z = 0.0001$ to 0.01 . We expect the difference to be even larger for more massive stars. For low mass progenitor the differences are smaller, but still not-negligible. For a star with an initial mass at $0.85M_{\odot}$ there is an increase in the white dwarf mass of $\sim 0.03M_{\odot}$ when the metallicity decreases from 0.001 to 0.0001 . Even if the differences in the final mass are not very large, the differences in the time spent during the stages previous to the white dwarf sequence will be, because the evolutionary time scales for low mass stars are very long. This age difference is important when we use evolutionary computations to estimate the age of stellar populations.

For comparison purposes, we include in Figure 4 observational data corresponding to open and globular clusters with a Main Sequence Turn Of mass in the range $\sim 0.8 - 4.0M_{\odot}$. We consider the data from two globular

Table 3. Results from our fittings for the initial and final masses for the white dwarf stars corresponding to five different clusters. Effective temperature and superficial gravity values for NGC 6819, NGC 7789 and Hyades are taken from Kalirai et al. (2014), for NGC 6791 are taken from Kalirai et al (2007), for NGC 6397 are taken from Moehler et al. (2004) and for M4 are from Kalirai et al. (2009).

Cluster	star	T_{eff} (K)	$\log g$	M_{WD}/M_{\odot}	$t_{\text{cool}}(\text{Myrs})$	$M_{\text{initial}}/M_{\odot}$
NGC 6397	WF4-358	18800 ± 340	7.72 ± 0.06	0.511 ± 0.023	75.75 ± 8	0.829 ± 0.030
M4	WD-00	20600 ± 600	7.75 ± 0.09	0.522 ± 0.027	52.89 ± 8	0.885 ± 0.011
M4	WD-04	24300 ± 500	7.68 ± 0.08	0.516 ± 0.028	27.48 ± 3	0.885 ± 0.011
M4	WD-06	25600 ± 500	7.87 ± 0.08	0.572 ± 0.036	21.08 ± 5	0.885 ± 0.011
M4	WD-15	24300 ± 600	7.79 ± 0.09	0.534 ± 0.039	27.29 ± 3	0.885 ± 0.011
M4	WD-20	19700 ± 600	7.73 ± 0.10	0.519 ± 0.038	58.83 ± 17	0.885 ± 0.011
M4	WD-24	25700 ± 500	7.70 ± 0.07	0.522 ± 0.018	22.32 ± 3	0.885 ± 0.011
NGC 7789	NGC 7798-5	31600 ± 200	7.89 ± 0.05	0.636 ± 0.024	8.66 ± 0.3	1.908 ± 0.051
NGC 7789	NGC 7798-8	25000 ± 400	8.06 ± 0.07	0.663 ± 0.037	26.15 ± 9	1.917 ± 0.051
NGC 6819	NGC 6816-6	21900 ± 300	7.89 ± 0.04	0.532 ± 0.017	43.15 ± 4	1.561 ± 0.050
NGC 6819	NGC 6816-7	16600 ± 200	7.97 ± 0.04	0.599 ± 0.010	141.63 ± 15	1.585 ± 0.054
Hyades	WD0325+096	14670 ± 380	8.30 ± 0.05	0.786 ± 0.030	357.59 ± 69	3.655 ± 0.692
Hyades	WD0406+169	15810 ± 290	8.38 ± 0.05	0.836 ± 0.019	337.26 ± 43	3.682 ± 0.536
Hyades	WD0421+162	20010 ± 320	8.13 ± 0.05	0.692 ± 0.028	97.75 ± 23	2.906 ± 0.109
Hyades	WD0425+168	25130 ± 380	8.12 ± 0.05	0.696 ± 0.027	30.48 ± 6	2.804 ± 0.109
Hyades	WD0431+126	21890 ± 350	8.11 ± 0.05	0.684 ± 0.028	61.76 ± 13	2.851 ± 0.096
Hyades	WD0437+138	15120 ± 360	8.25 ± 0.09	0.757 ± 0.055	305.00 ± 59	3.498 ± 0.377
Hyades	WD0438+108	27540 ± 400	8.15 ± 0.05	0.717 ± 0.028	17.65 ± 5	2.785 ± 0.083
Hyades	WD0348+350	14820 ± 350	8.31 ± 0.05	0.792 ± 0.029	363.95 ± 73	3.836 ± 0.709
Hyades	HS0400+1451	14620 ± 60	8.25 ± 0.01	0.756 ± 0.068	325.17 ± 23	3.612 ± 0.403
Hyades	WD0625+415	17610 ± 280	8.07 ± 0.05	0.654 ± 0.027	137.70 ± 21	2.967 ± 0.106
Hyades	WD0637+477	14650 ± 590	8.30 ± 0.06	0.786 ± 0.036	361.94 ± 111	3.824 ± 0.923
NGC 6791	WD7	14800 ± 300	7.91 ± 0.06	0.565 ± 0.030	196.66 ± 40	1.166 ± 0.028

clusters, M4 and NGC 6397, and four open clusters, NGC 6791, NGC 6819, NGC 7789 and Hyades. The cluster and star identifications and the spectroscopic parameters for the star sample are listed in the first four columns of Table 3. Effective temperature and superficial gravity values were taken from the works of Kalirai et al. (2014) for NGC 6819, NGC 7789 and Hyades, from Kalirai et al. (2007) for NGC 6791, from Moehler et al. (2004) for NGC 6397 and from Kalirai et al. (2009) for M4. These spectroscopic parameters were derived from the well know technique which involves fitting the Balmer lines shape of the spectrum to model atmospheres (e.g. Bergeron et al. 1992). With T_{eff} and $\log g$ constrained, we estimated the spectroscopic mass values (column 5 of Table 3) by a linear interpolation of carbon–oxygen core cooling tracks in the $\log g - T_{\text{eff}}$, computed from full evolutionary models. The cooling ages (t_{cool}) for the white dwarf stars were extracted also from our evolutionary tracks (column 6 from Table 3). By subtracting t_{cool} from the total age of the cluster, we obtained the lifetime of the progenitor star (t_{prog}) at the point of highest temperature in the post-AGB stage, before entering the white dwarf cooling curve. We assumed that the total ages of the clusters are 2.5 ± 0.2 Gyr for NGC 6819 and 1.4 ± 0.1 Gyr for NGC 7789 (Kalirai et al. 2001, 2008), 625 ± 50 Myrs for the Hyades (Perryman et al. 1998; Claver et al. 2001), 8.5 ± 0.5 Gyr for NGC 6791 (Kalirai et al. 2007), 11.7 ± 0.3 Gyr for NGC 6397 (Hansen et al. 2013) and 11.6 ± 0.6 Gyr for M4 (Bedin et al. 2009). The initial mass values (last column of Table 3) have been computed directly from the pre-white dwarf lifetime t_{prog} , using the mass-lifetime relations from pre-white dwarf theoretical evolutionary models. For each cluster we take into

account the metallicity value and consider a grid of progenitor sequences with the closest Z to compute the initial mass from the progenitor age.

Note that there is a good agreement between theoretical IFMR and the semi empirical values. In general, all the points representing the star sample listed in Table 3 are accounted for by the range covered by our theoretical curves, within the metallicity range considered by our computations. Then, the spread observed in the data can be solved by considering a spread in the metallicity values. A more detailed analysis of Figure 4 shows that for stars belonging to M4 and NGC 6397, at the low mass limit, and to the Hyades, for high mass values, the theoretical curves with the right metallicity fits the points within the uncertainties. For NGC 6819, the data is better represented with somewhat lower metallicities than the listed observational value $Z = 0.017$. However, asteroseismic inferences from red giants stars from this cluster suggest that metallicity might be significantly lower than solar, between $Z = 0.0033$ and $Z = 0.008$ (Hekker et al. 2011). For the very metal rich open cluster NGC 6791, represented by a single object WD7, and the near solar metallicity open cluster NGC 7789, the accordance between the semi empirical data and the theoretical IFMR is poor. For NGC 7789 the metallicity value $Z = 0.014$ is an average of literature values obtained by means of different photometric and spectroscopic techniques (see Wu et al. 2007), ranging from $Z = 0.0085$ ($[Fe/H] = -0.35$) to solar ($\sim Z = 0.019$). Our results would be in better agreement with a metallicity value closest to the lower limit ~ 0.008 . In the case of NGC 6791 we expect a higher mass–loss rate given its high metallicity. How-

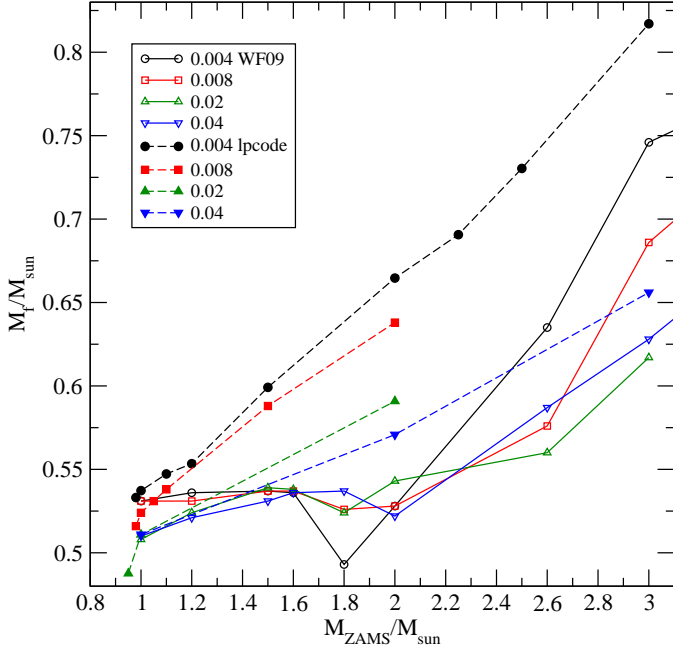


Figure 5. Theoretical Initial-to-Final mass relation for sequences with metallicity values $Z = 0.004$ (black circles), $Z = 0.008$ (red squares), $Z = 0.02$ (green triangles up) and $Z = 0.04$ (blue triangles down). Hollow symbols correspond to the results of Weiss & Ferguson (2009) while fill symbols correspond to results obtained in this work – see text for details. We consider the initial mass range where the two studies overlap. (A color version of this figure is available in the on-line journal.)

ever the final mass obtained for WD7 is around $\sim 0.03M_{\odot}$ higher than the expected value, indicating that the theoretical mass-loss rates at high metallicity values should be smaller than assumed, in agreement with the results obtained by Miglio et al. (2012) for this cluster. In summary, different metallicity values of the progenitor stars leads to different final masses on the white dwarf cooling curve, causing the observed spreading.

4.1 Comparison with theoretical and semi-empirical IFMR

In this section we compare our results with other theoretical determinations of the IFMR performed using independent evolutionary codes. In particular our definition of the final mass is the real mass of the white dwarf star at the cooling curve and not the mass of the hydrogen free core at the first thermal pulse. As it was shown by Kalirai et al. (2014) the mass of the core increases during the TP-AGB, resulting in a final mass larger than the one at the first thermal pulse. Therefore we select theoretical computations that consider the AGB evolution in the definition of the IFMR to compare with our results.

Weiss & Ferguson (2009) computed sequences from the ZAMS to the end of the TP-AGB for 5 values of metallicity between $Z = 0.0005$ and $Z = 0.04$ and initial masses ranging from $1.0 M_{\odot}$ to $6.0 M_{\odot}$. We compare our results with those of Weiss & Ferguson (2009) in Fig. 5. Only the metallicity val-

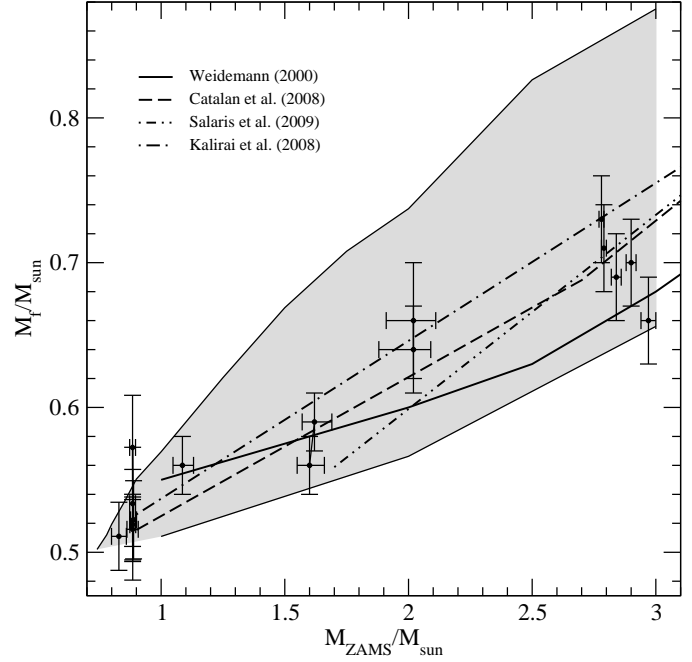


Figure 6. Theoretical Initial-to-Final mass relation computed in this work (gray area) compare to the semi-empirical relations from Weidemann (2000, full line), Catalán et al. (2008, dashed line), Salaris et al. (2009, dashed-dot-dot line) and Kalirai et al. (2008, dashed-dot line).

ues and the initial mass range where both studies overlap are plotted. At the low mass end we have good agreement, specially for high metallicity progenitors. Differences are more important for high mass stars and low metallicity progenitors. In their calculation, envelope overshooting was allowed during the TP-AGB, with $f = 0.016$ for all sequences. This overshooting prescription leads to an enhanced reduction of the final core mass, leading to an IFMR very close to the relation between the initial mass and the core mass at the first thermal pulse. Note the minimum in the final mass for Weiss & Ferguson (2009) around $\sim 2M_{\odot}$ corresponding to the limit between the sequences that experience an helium flash at the beginning of the central helium burning phase, and those that do not (see section 3.2). This minimum is also present in our computations when we consider the mass of the hydrogen free core at the first thermal pulse as the final mass (see Renedo et al. 2010).

Other authors (e.g. Karakas 2010; Marigo & Girardi 2007; Marigo et al. 2013) have computed detailed atmosphere models of TP-AGB evolution, considering parametrized overshooting treatments and also a detailed composition of the surface. They calibrate the dredge-up onset and efficiency with observations of carbon surface abundances of AGB stars. Because in Karakas (2010) and Marigo & Girardi (2007) the authors consider dredge-up episodes during the TP-AGB we expect final mass for sequences with initial masses above $\sim 2M_{\odot}$ to be higher in our computations. We showed in section 3.3 that for $Z \sim 0.02$ our final masses can be overestimated by less than 10%, while for lower metallicity this difference can reach $\sim 20\%$.

Karakas (2010) computed a large grid of TP-AGB models covering the metallicity range between $Z = 0.0001$ and $Z = 0.02$, and initial masses between 1 and $6M_{\odot}$. She considered a detailed treatment of the third dredge-up in order to reproduce the atmospheric carbon abundances observed in field stars. As we expected, for initial mass larger than $\sim 1.8 - 2.0M_{\odot}$ we obtain final masses larger than those of Karakas (2010), up to a $\sim 12\%$ for $Z = 0.0001$ and $M_{\text{initial}} = 3M_{\odot}$. For low initial masses our models show significantly lower final masses than that of Karakas (2010), up to $\sim 27\%$ for $1M_{\odot}$ and $Z = 0.0001$. This large difference can be mainly due to the lack of mass loss during the pre-AGB evolution adopted for the initial models. As in Wiess & Ferguson (2009), we consider mass loss during the RGB phase modeled by the Reimers formulae (Reimers 1975). Therefore our sequences begin the AGB evolution with a smaller mass than that of the ZAMS, limiting also the number of thermal pulses and thus, the growth of the hydrogen free core during the TP-AGB. Similar results to those of Karakas (2010) are found when we compare our IFMRs with those of Marigo & Girardi (2007). They also computed detailed models for TP-AGB evolution for $Z = 0.0001$ to $Z = 0.03$ and $M_{\text{initial}} = 0.5 - 5.0M_{\odot}$, calibrating the onset and the efficiency of the third dredge-up with observations, such as carbon star luminosity functions in the Magellanic Clouds and TP-AGB lifetimes in Magellanic star clusters. The initial models at the first thermal pulse are taken from Girardi et al. (2000), derived again from constant mass computations. They still find a significant dependence with metallicity, leading to an allowed final mass range of $0.1M_{\odot}$ wide for a given initial mass (see their figure 26).

Finally, Kalirai et al. (2014) found a grid of best fit models from the model grid of Marigo et al. (2013), therefore without mass loss in the RGB, for $Z = 0.02$ that better represents the core mass growth during the TP-AGB for solar metallicity in the initial mass range of $1 - 4.4M_{\odot}$. The adopted dredge-up efficiencies varies with the initial mass. From their best-fitting TP-AGB models we can extract an IFMR (see their Table 3) and compare their predictions with ours. As a result, we found that the final masses from Kalirai et al. (2014) are somewhat larger than ours in the whole initial mass range. The differences are small, up to $\sim 4\%$ compared to our $Z = 0.01$ grid, and $\sim 8\%$ as compared to our $Z = 0.02$ models. The smaller differences are for initial mass around $2.5M_{\odot}$, where dredge-up efficiencies are larger for this metallicity.

In addition to theoretical computations, several studies where dedicated to determine a semi-empirical IFMR from observations of star belonging to globular and open clusters and binary systems on the Galactic field. We selected the semi-empirical IFMR from Catalán et al. (2008b), Salaris et al. (2009) and Kalirai et al. (2008) to compare with our theoretical results. We also include the classical semi-empirical IFMR from Weidemann (2000). The results are shown in Figure 6. Most of the semi-empirical results fall between our theoretical IFMR characterized by $Z = 0.004$ and $Z = 0.02$. At the low mass end, below $\sim 1.7M_{\odot}$, the IFMR of Catalán et al. (2008b) and Kalirai et al. (2009) fall between the $Z = 0.004$ and $Z = 0.01$ curves. Salaris et al. (2009) IFMR is better matched by our $Z = 0.02$ curve. At the high mass

end, the semi-empirical IFMR are better matched by considering metallicity values between $Z = 0.008$ and $Z = 0.01$. This is a consequence of the sample used to determine the IFMR, corresponding to younger, and more metallic open clusters, and common proper motion pairs from the solar vicinity. In particular, Kalirai et al. (2008) extended the low mass end towards lower initial masses by including the old metal-rich open cluster NGC 6791. In all cases, the semi-empirical IFMR demonstrate that lower mass main sequence stars produce lower mass white dwarf stars (Kalirai 2013).

5 WHITE DWARF MODELS AND THE METALLICITY DEPENDENCE

5.1 Hydrogen envelope thickness

As shown by Iben & MacDonald (1986) –see also Renedo et al. (2010); Miller Bertolami et al. (2013)– the amount of hydrogen left in a white dwarf star is metallicity dependent, being thicker for models with less metallic progenitors. As a result of the larger hydrogen envelopes, residual H burning is expected to become more relevant in white dwarf stars with low metallicity progenitors. Results from Miller Bertolami (2013) showed that for metal poor stars ($Z \sim 0.0001$), the luminosity is completely dominated by nuclear burning, even at rather low luminosities. This leads to a significant delay in the cooling times, as compared to stars with higher metallicities, such as $Z = 0.01$, in which nuclear burning does not play a leading role, and most of the energy release come from the thermal energy stored in the interior. From the top panel of Figure 7, where we show the total hydrogen content in solar units in terms of the white dwarf mass at the point of maximum effective temperature, we see that, in general, a lower hydrogen content is found for a higher metallicity value for the progenitor star. Some departures of the expected trend can be noticed from this figure also. For instance, the change in the slope for high mass $Z = 0.0001$ models is due to the occurrence of the third dredge-up for the two more massive models, as also shown in Figure 1 of Miller Bertolami (2013). For $Z = 0.001$, the hydrogen content for the $0.627M_{\odot}$ model is lower than that of the $Z=0.004$. The largest departures from the general trend are found for low mass white dwarfs, in particular those with stellar masses below $\sim 0.53M_{\odot}$. As we mention in sec. 3.1, sequences with the lowest masses of the grid experience hydrogen sub-flashes before entering its final cooling track. In particular, the sequence with initial metallicity $Z = 0.02$ and white dwarf mass $0.488M_{\odot}$ experience a late thermal pulse which significantly reduce the amount of hydrogen left in the star (Althaus et al. 2005b).

As residual hydrogen burning is active, the mass of the hydrogen content decreases, until it reaches a certain value ($\sim 8 \times 10^{-5}M_{\odot}$ for solar metallicity stars, Renedo et al. 2010) where the pressure at the bottom of the envelope is not large enough to support further nuclear reactions, and the hydrogen content reaches a stationary value. In addition, time-dependent chemical diffusion builds a pure hydrogen envelope when the star reaches lower effective temperatures ($\sim 30\,000$ K for solar metallicity). Then, at late stages of the cooling, a smoother distribution of the hydrogen mass

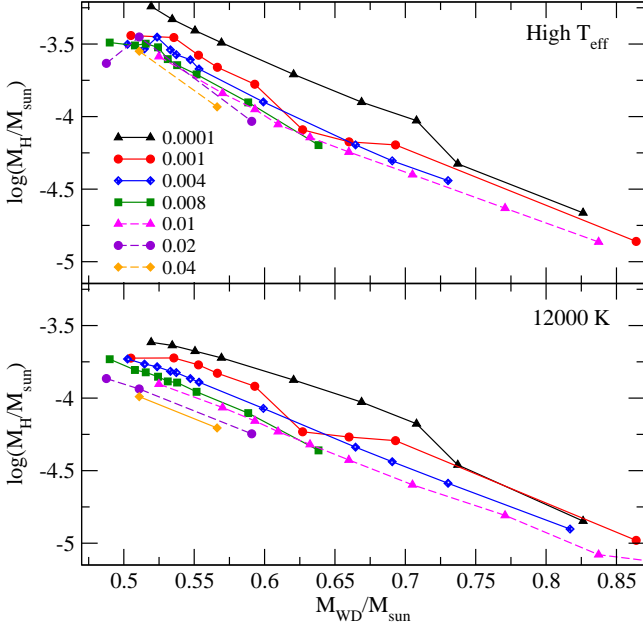


Figure 7. Hydrogen mass at the cooling sequence as a function of the white dwarf mass, at the point of maximum effective temperature at the beginning of the white dwarf cooling branch (top panel) and for models at late stages on the white dwarf cooling curve, with effective temperature ~ 12000 K. Each curve corresponds to a different initial metallicity (see references on the plot). A color version of this figure is available in the on-line journal.

in terms of the stellar mass and metallicity can be expected. This can be seen for our model grid from the bottom panel of Figure 7, where we depict the total hydrogen mass as a function of the white dwarf mass at ~ 12000 K. In particular, at the low mass end, the hydrogen envelope mass clearly decreases as the initial metallicity increases.

A comparison between the resulting hydrogen content for a fixed white dwarf mass shows a spread with metallicity. For instance, for a white dwarf with a stellar mass of $\sim 0.570M_{\odot}$ we found that the reduction of the hydrogen content due to an increase in the initial metallicity from $Z = 0.001$ to $Z = 0.04$ can be up to a factor of 2. This difference is small and does not introduce a measurable difference on the cooling time scale at low luminosities. However we must take into account that the hydrogen content resulting from canonical evolutionary computations is a higher limit. Asteroseismological studies show that the mean hydrogen mass for pulsating ZZ Cetus stars is $\sim 10^{-6}M_{*}$, around two orders of magnitude lower than the canonical values for most of the sequences computed in this work (Castanheira & Kepler 2009; Romero et al. 2012, 2013).

5.2 Central oxygen abundances

Figure 8 displays the central oxygen abundance by mass left after core helium burning in terms of the white dwarf mass for three metallicity values $Z = 0.0001$, $Z = 0.004$ and $Z = 0.01$. The numbers in the figure indicate the mass of the progenitor star for some points. The predictions of our calculations for $Z = 0.01$ are in good qualitative agreement with

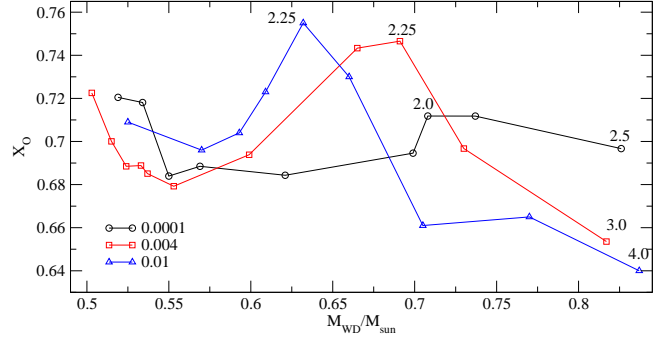


Figure 8. Central oxygen abundance in terms of the white dwarf mass, for three metallicities, $Z = 0.0001$ (black circles), $Z = 0.004$ (red squares) and $Z = 0.01$ (blue triangles). The values are taken after rehomogenization but before crystallization sets in the central core. The numbers indicate the progenitor mass at the ZAMS for some points.

the computations of Salaris et al. (1997) for solar metallicity, as shown in Althaus et al. (2010). We recall that the final carbon–oxygen stratification of the emerging white dwarf depends on both the efficiency of the $^{12}\text{C}(\alpha, \gamma)^{16}\text{O}$ reaction rate and the occurrence of extra–mixing episodes toward the late stages of core helium burning. Note that for all sets, a maximum in the oxygen abundance is predicted, being the mass of the white dwarf model larger for lower metallicity values. However, when we consider the initial mass, we found that the maximum is located approximately at the same value, around $2.25M_{\odot}$ for $Z = 0.004$ and $Z = 0.01$ and around $2M_{\odot}$ for $Z = 0.0001$. This maximum is also present in Salaris et al. (1997) models. After that, the oxygen abundance decreases and tends to a stable value oscillating between 0.61 and 0.63, as also shown in Romero et al. (2013) for white dwarf models with $Z = 0.01$. Finally, note that the changes in the oxygen and carbon central abundances due to metallicity can get up to $\sim 10\%$ in the metallicity range shown in Fig. 8.

6 THE AGE OF STELLAR POPULATIONS AND THE METALLICITY PARAMETER

As it is known, the age of the model before entering the final cooling sequence is metallicity dependent; for a given progenitor mass on the ZAMS, the age of the pre-WD star at the point of maximum effective temperature is significantly smaller for lower metallicities. For progenitor stars corresponding to initial masses above $\sim 1.5M_{\odot}$, the evolutionary scales are small, from 2 Gyr to hundreds of Myr. But for low mass stars, those that present a fraction of its core in a degenerate state after central hydrogen exhaustion, the evolutionary scales are much longer, and can reach 15 Gyr. In addition, for low mass stars the time spent on the RGB phase is not negligible and can reach up to $\sim 2 - 3$ Gyr for $\sim 1M_{\odot}$. Thus the metallicity dependence of the pre-WD age will be more important for low mass sequences and older populations like globular clusters. We can see from Table 1 that the pre-WD age of a $1M_{\odot}$ progenitor star is reduced from 12.5 Gyr to 5.9 Gyr when the metallicity goes from a solar

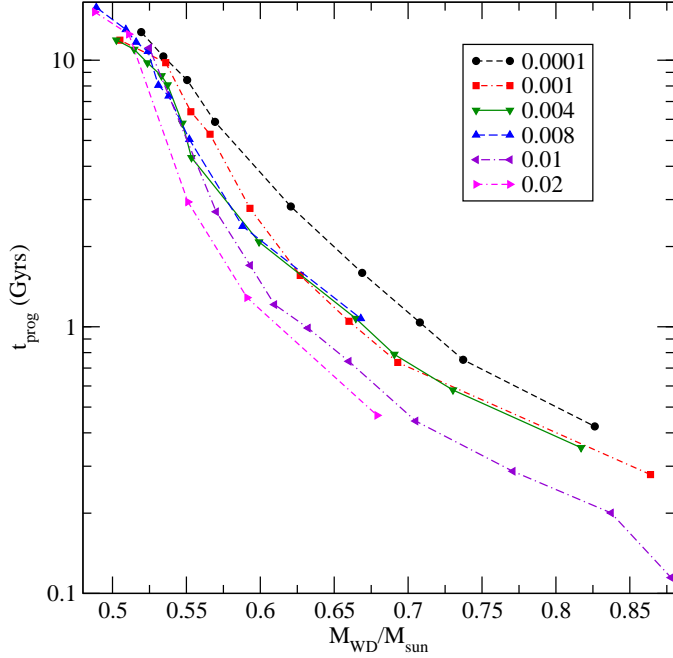


Figure 9. Lifetime previous to the white dwarf stage versus stellar mass on the cooling curve. Each curve corresponds to a single initial metallicity. (A color version of the figure is available on the on-line version).

value ($Z = 0.02$) to very metal poor values characteristic of halo population ($Z = 0.0001$).

Figure 9 shows the pre-WD age (t_{prog}) in terms of the white dwarf mass for all metallicity values considered in this work. The general trend shows that the age, for a given stellar mass, decreases with metallicity (e.g. Isern et al. 2005). When the step on metallicity is sufficiently small, we can notice a departure from the general trend, caused by the difference in the progenitor mass. As it was shown in section 4, the mass of the resulting white dwarf star decreases when metallicity increases (see Table 1). This is a consequence of an enhanced mass loss rate with increasing metallicity during the giant stages. Note that the metallicity dependence of the final mass will still be present if we were to consider the mass of the hydrogen free core at the first thermal pulse, since the mass of the carbon-oxygen core after helium burning increases with decreasing metallicity, as shown in Figure 3. Two effects are present having opposite influences. For a fixed white dwarf mass, the lifetime of the progenitor star decreases with metallicity but, on the other, the mass of the progenitor is smaller and its lifetime increases (e.g. Isern et al. 2005). For a low mass white dwarf, the age difference can be as high as 8 Gyr.

In Figure 10 we show the age of the progenitor star in terms of the initial metallicity. From this figure the differences on the white dwarf total age due to metallicity is clearer. We found that the age decrease for low Z but the dependence is not always monotonous, indicating the influence of another parameter, i.e. the IFMR. As the stellar mass increases, the pre-WD lifetime is shorter, and usually

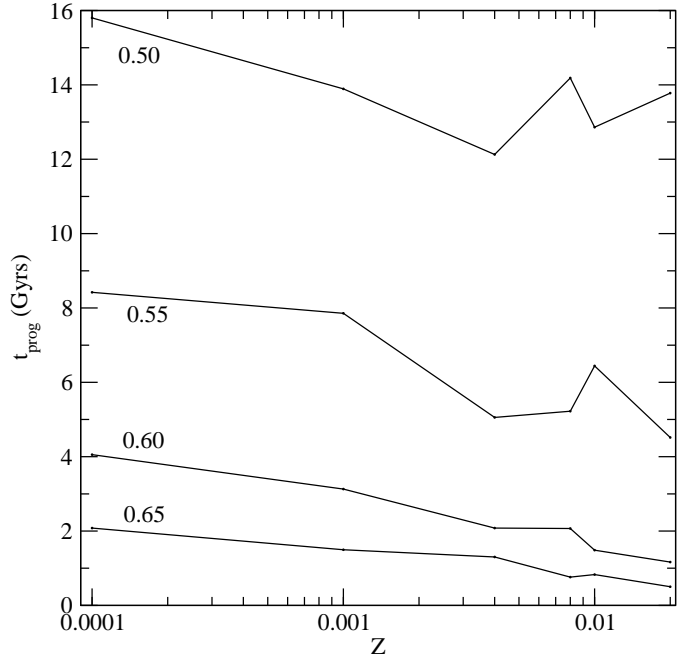


Figure 10. Pre-WD lifetime in terms of the initial metallicity for white dwarf models with masses 0.50 , 0.55 , 0.60 and $0.65M_{\odot}$.

negligible, as compared to the cooling time on the white dwarf sequences once they evolved to lower luminosities.

We can do a simple exercise by estimating the total age of a typical halo globular cluster. Kalirai et al. (2009) determined spectroscopically that the mass for the bright white dwarf stars in M4, at the beginning of the observed cooling sequence, is $0.592 \pm 0.012M_{\odot}$. Assuming that we do not know the metallicity of the cluster, we can estimate the age of the progenitor, and of the star, from the pre-WD ages listed in Table 1. The results are listed in Table 4, along with the estimated mass of the progenitor star. Note that all progenitor masses are low mass stars and do not experience many thermal pulses, between 1 and 5, during the AGB. The pre-WD age does not decrease monotonously, as we saw from Figs. 9 and 10. For the metallicity value estimated spectroscopically for M4, $Z \sim 0.001$, the estimated values of progenitor mass for the bright white dwarfs is in agreement with the estimations of the stellar mass of the main sequence turn off, $\sim 0.85M_{\odot}$ (see Sec. 6.1).

6.1 The white dwarf cooling curve in globular clusters

In Figure 11 we show the total luminosity as a function of age during the white dwarf cooling sequences for four different metallicity values $Z = 0.0001, 0.001, 0.004$ and 0.008 . For each sequence we consider the total age of the star, i.e. the age measured from the ZAMS considering all previous stages to the white dwarf cooling curve, added to the cooling lifetime. The mass range for each metallicity is indicated in the plot. Finally, the horizontal dashed line represents the point in the cooling curve where crystallization in the central core begins, following of the Horowitz et al. (2010) prescrip-

Table 4. Age and progenitor mass for different metallicities for a white dwarf star with mass $0.592 \pm 0.012 M_{\odot}$, estimated by Kalirai et al. (2009) for the bright white dwarf stars of M4.

Z	Age [Gyr]	M_{ZAMS}/M_{\odot}
0.0001	11.133	0.83
0.001	10.587	0.90
0.004	9.196	0.97
0.008	8.834	1.03
0.01	10.369	1.04
0.02	7.499	1.36
0.04	9.413	1.22

tion of the C–O phase diagram. The white dwarf sequences characterized by a progenitor metallicity of $Z = 0.001$ and $Z = 0.01$, originally computed in Renedo et al. (2010), were recalculated by considering the Horowitz et al. (2010) phase diagram. Note that with the Segretain & Chabrier (1993) phase diagram in the evolutionary computations, the effective temperature at which crystallization begins at the center of the star is ~ 1000 K higher than that predicted by Horowitz et al. (2010) (see Romero et al. 2013 for details). Although white dwarf atmospheres at late stages of the cooling sequences are metal free, the final white dwarf evolution is not insensitive to the metallicity of the progenitor star. As we showed in previous sections, the pre-WD lifetime is larger for metal rich sequences as compared to low metallicity progenitors. In case of a $1M_{\odot}$ progenitor star, the progenitor lifetime goes from 5.9 Gyr to 11.1 Gyr when the initial metallicity increases from $Z = 0.0001$ to $Z = 0.01$. On the other hand, as we showed in sec. 5.1, the total amount of hydrogen left in the white dwarf remnant is usually larger for lower metallicities, so a thicker hydrogen layer is expected for low Z sequences.

Our lifetime computations during the white dwarf sequences are consistent to those of BaSTI evolutionary code up to 2% at luminosities lower than $\log(L/L_{\odot}) \sim -1.5$ (Salaris et al. 2013). This difference is smaller than the uncertainties in cooling times attributable to the present uncertainties in the white dwarf chemical stratification. We also computed sequences with an initial mass $1M_{\odot}$ and metallicity of $Z = 0.0001$ and $Z = 0.02$ using MESA (Paxton et al. 2011, 2013) and found lifetimes consistent with ours, with differences of ~ 0.1 Myr at ~ 25000 K on the cooling curve.

HST observations of globular clusters in the Galactic Halo, M4 (Richer et al. 2004; Hansen et al. 2004), NGC 6397 (Richer et al. 2006; Hansen et al. 2007) and 47 Tuc (Hansen et al. 2013), have uncovered several hundred member white dwarf stars. From a sample of galactic globular clusters, Krauss & Chaboyer (2003) derived an mean age of $12.6^{+3.4}_{-2.2}$ Gyr. More recently, Kalirai (2012) derived an age of the stellar halo near the position of the Sun to be 11.4 ± 0.7 Gyr. Consequently, given these large ages, bright white dwarf stars are expected to have low stellar mass values around $0.51 - 0.55M_{\odot}$ (Renzini & Fusi Pecci 1988; Renzini et al. 1996). With the high precision data available we can employ the current observational constrains on age to derive some properties for the white dwarf sample in these

systems. In particular, we used the total age determinations of three globular clusters to estimate the mass range on the white dwarf cooling curve and the minimum mass expected to have some fraction of its core in a crystallized state.

The globular cluster NGC 6397 is one of the closest globular clusters (2.6 kpc) and is also a metal poor system with a iron to hydrogen ratio of $[\text{Fe}/\text{H}] = -2.00 \pm 0.01$, corresponding to $Z = 0.0001$. For this globular cluster Hansen et al. (2013) determined a total age of 11.7 ± 0.3 Gyr. Considering this total age we found that the white dwarf stars at high luminosities at the beginning of the cooling curve are characterized by a mean mass of $0.535 \pm 0.008M_{\odot}$ corresponding to an initial mass of $\sim 0.85M_{\odot}$. On the other hand, the corresponding minimum stellar mass for a white dwarf to have undergone some degree of crystallization in the central core, as seen by Winget et al. (2009, 2010), is $0.561 \pm 0.007M_{\odot}$, with a progenitor mass of $\sim 0.95M_{\odot}$. The observed white dwarf mass is not the same along the cooling curve. White dwarf stars with higher stellar mass cool faster, having lower luminosity values at a given age. In addition, the pre-white dwarf lifetime decreases dramatically when the progenitor mass increases, so these stars reach the white dwarf stage in a shorter amount of time.

For M4, Hansen et al. (2004) derived an age of 12.1 Gyr, with a 95% lower bound of 10.3 Gyr, by direct fitting of the Color–Magnitude Diagram. Bedin et al. (2009) also determine the cluster age of 11.6 ± 0.6 Gyr, consistent with the age from fits to the main–sequence turnoff (12.4 ± 1.4 Gyr). The iron to hydrogen fraction for M4 is $[\text{Fe}/\text{H}] = -1.1 \pm 0.01$ (Mucciarelli et al. 2011) corresponding to $Z = 0.0013$. We consider that the grid of sequences with $Z=0.001$ is representative of this cluster. By considering the age determinations from Bedin et al. (2009) we found that the mass at the top of cooling curve is around $\lesssim 0.536 \pm 0.015M_{\odot}$, in agreement with the mass determinations of Kalirai et al. (2009) of $0.529 \pm 0.012M_{\odot}$. Note that the progenitor mass for a white dwarf with $\sim 0.536M_{\odot}$ is $\sim 0.92M_{\odot}$ at $Z = 0.001$. Also, those sequences with white dwarf mass $\gtrsim 0.553 \pm 0.008M_{\odot}$ have reached crystallization temperatures at an age ~ 11.6 Gyr. So sequences with initial mass larger than $1M_{\odot}$ are already crystallized. The small difference between the age derived by Bedin et al. (2009) and that of Hansen et al. (2004) do not change considerably our results.

The globular cluster 47 Tuc is more metal rich than both NGC 6397 and M4, with $[\text{Fe}/\text{H}] = -0.75$ (Carretta et al. 2009), so we use a metallicity value of $Z = 0.004$ for this cluster. Hansen et al. (2013) determine a cluster age by fitting the properties of the cluster white dwarf population. They derived a total age of 9.9 ± 0.7 Gyr at 95% confidence. From our computations we found that the sequence characterized by a white dwarf mass of $0.537M_{\odot}$ has not reached the crystallization temperature (see Fig. 11) while all sequences with white dwarf mass $\geq 0.547M_{\odot}$, and progenitor mass of $\geq 1.1M_{\odot}$, have a partially crystallized core at 10 Gyr. Finally the white dwarf stars at high luminosity in the cooling curve are characterized by an stellar mass around $0.524 \pm 0.005M_{\odot}$ corresponding to progenitors with $0.95M_{\odot}$.

Summarizing, the stellar mass values of the white dwarf stars at high luminosities derived for the three globular clusters are very similar, around $\sim 0.53M_{\odot}$, in agreement with

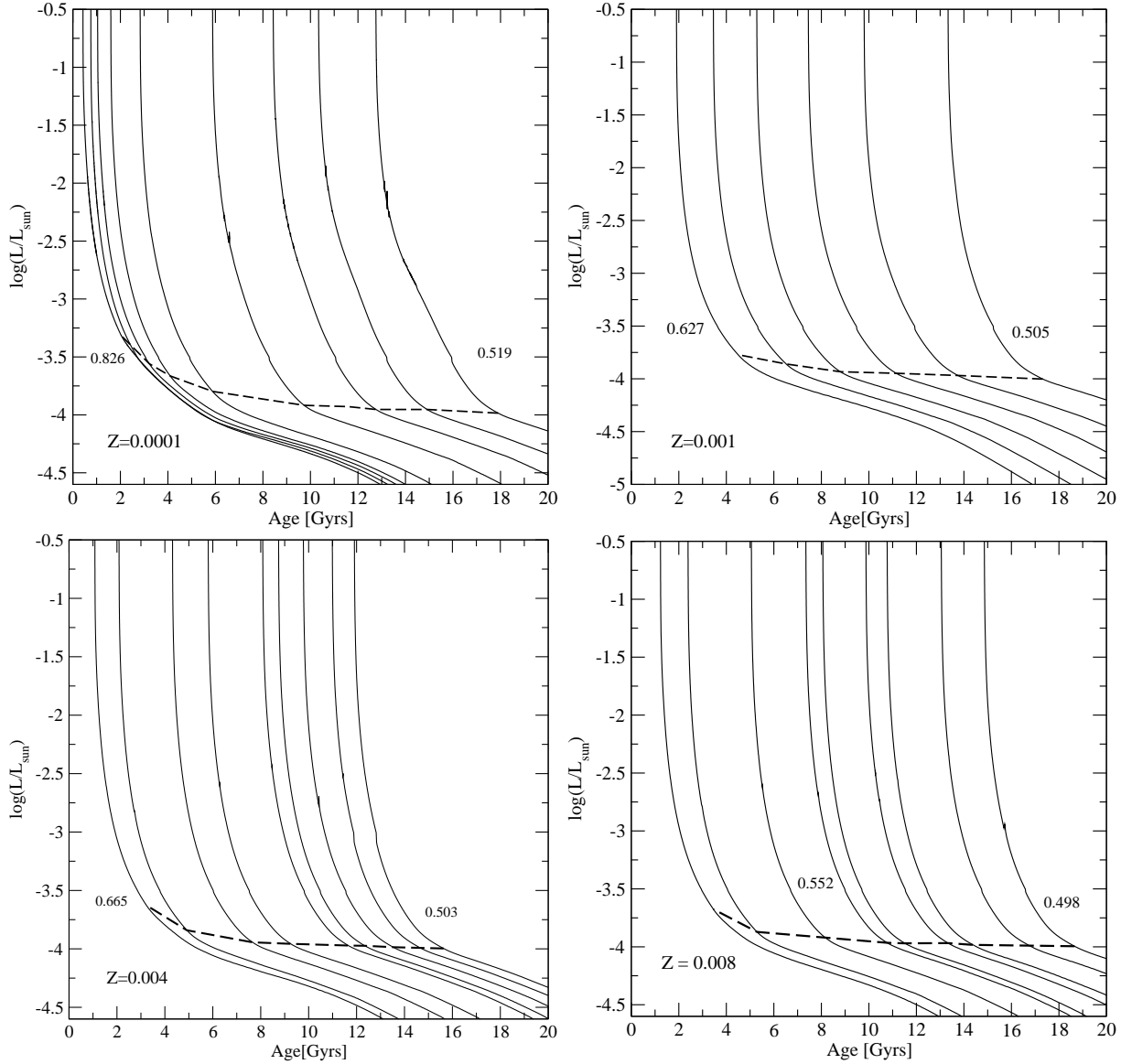


Figure 11. Total luminosity as a function of age for our set of sequences with four different metallicity of the progenitor star. The age corresponds to the total age of the model, by considering all the stages previous to the white dwarf cooling. The horizontal dashed line represents the point in the evolution where the crystallization process begins at the core, by means of the Horowitz et al. (2010) phase diagram for crystallization. The stellar mass values in solar mass units, from left to right, are: 0.519, 0.534, 0.550, 0.561, 0.569, 0.621, 0.669, 0.708, 0.737 and 0.826 for $Z = 0.0001$, 0.505, 0.536, 0.553, 0.566, 0.593, 0.627 for $Z = 0.001$; 0.503, 0.515, 0.524, 0.533, 0.537, 0.547, 0.553, 0.599 for $Z = 0.004$ and 0.498, 0.509, 0.516, 0.524, 0.531, 0.538, 0.552, 0.588 for $Z = 0.008$.

previous estimates. Nevertheless, the progenitor mass at the ZAMS changes with metallicity. The progenitor mass for NGC 6397 is around $0.85M_{\odot}$, while for M4 is $\sim 0.92M_{\odot}$. Since the total ages for these two systems are basically the same, within the uncertainties, the initial mass differences are a consequence of the different characteristic metallicities. 47 Tuc is younger than NGC 6397 and M4 by $\sim 1 - 2$ Gyr and thus the mass of the main sequence is larger ($0.95M_{\odot}$), as expected. However the stellar mass at high luminosities in the white dwarf cooling sequences is the lowest of the sample, indicating an enhanced mass loss rate, associated also to the higher metallicity.

7 CONCLUSIONS

In this work we studied the impact of metallicity on the theoretical white dwarf models, considering also its influence on the previous stages of evolution through the analysis of the IFMR and the evolutionary lifetimes. To this end we compute a grid of full evolutionary sequences characterized by metallicity values for the progenitor stars between $Z = 0.0001$ and 0.04 , covering the Z range observed on the galactic disk and halo populations. We focused on stars with initial masses ranging from $0.85M_{\odot}$ to $3M_{\odot}$, giving rise to white dwarf stellar masses in the range between $\sim 0.5M_{\odot}$ to $\sim 0.87M_{\odot}$. Our main results are the following:

- From our theoretical evolutionary computations, we found that the IFMR shows a dependence with the initial metallicity: the stellar mass of the remnant on the white dwarf colling curve decreases as the initial metallicity increases, indicating an strong influence of the metallicity on the mass loss rates during the RGB and the AGB phases. Our results are in good agreement with observations and semi empirical estimations of the IFMR, showing that the spread observed in the semi empirical data can be explain by means of the different metal abundances.

Our analysis on the IFMR does not include the effect of extra-mixing episodes during the TP-AGB evolution. Then for most sequences dredge-up episodes, and its effects on the effective temperature, mass-loss rate, and core mass growth during the TP-AGB evolution, are not present. It follows that the dependence of the IFMR is explored mainly under the conditions of fixed initial metallicity, and photospheric C/O ratio below unity during the TP-AGB phase, and thus no C-rich stars are formed from our models, except for sequences with high initial mass and metallicity $Z = 0.0001$.

- The mass of the helium core at the beginning of the central helium burning is smaller for more metal rich models. This will strongly influence the determination of the inner chemical composition of white dwarf stars with stellar mass $\sim 0.5M_{\odot}$. Finally, the minimum mass for a star to undergo a helium flash decreases with metallicity.

- We confirm the dependence with metallicity of the hydrogen mass left at a white dwarf star, being in general thinner for models with higher Z progenitors.

- We found that as the metallicity increases the pre-white dwarf lifetimes also increases, with age differences up to $\sim 5 - 6$ Gyr for a $\sim 1M_{\odot}$ star. Then, in order to estimate the age of a stellar population or a single object properly, we not only need to consider the total pre-white dwarf lifetime but also we must take into account its characteristic metal content.

- Finally we employed our evolutionary computations to study three old globular clusters characterized with very different metallicity values: NGC 6397 ($Z = 0.0001$), M4 ($Z = 0.001$) and 47 Tuc ($Z = 0.004$). By taking the age determinations from the literature, we estimate the mass of the white dwarf at high luminosities and the corresponding mass of the progenitor star, employing the IFMR with the corresponding Z value. We found that all three clusters have a similar white dwarf mass at high luminosities ($\sim 0.53M_{\odot}$), in agreement with previous estimates. However, the initial mass values are different, being larger for 47 Tuc. This result is an indication of the dependence of IFMR with the metallicity.

In future works an extension to higher initial masses should be performed, from the theoretical point of view in order to study younger stellar populations, as open clusters. Also, this could be used to constrain the free parameters governing the theoretical mass loss rates that are currently used in stellar evolutionary computations.

ACKNOWLEDGMENTS

Part of this work was supported by CNPq-Brazil and FAPERGS-Pronex Brazil. We thank the anonymous referee for their useful comments and suggestions. A.D. Romero thanks L. Althaus, D. Koester and J. Isern for very useful discussion on this work. This research has made use of NASA's Astrophysics Data System.

REFERENCES

- Althaus, L.G., Serenelli, A.M., Córscico, A.H., & Montgomery, M.H. 2003, *A&A*, 404, 593
- Althaus, L. G., Serenelli, A. M., Panei, J. A., et al. 2005a, *A&A*, 435, 631
- Althaus, L. G., Miller Bertolami, M. M., Córscico, A. H., García-Berro, E., & Gil-Pons, P. 2005b, *A&A*, 440, L1
- Althaus, L. G., García-Berro, E., Isern, J., Córscico, A. H., & Rohrmann, R. D. 2007, *A&A*, 465, 249
- Althaus, L. G., Córscico, A. H., Bischoff-Kim, A., et al. 2010, *ApJ*, 717, 897
- Althaus, L.G., García-Berro, E., Isern, J., Córscico, A.H., & Miller Bertolami, M.M. 2012, *A&A*, 537, A33
- Althaus, L. G., Miller Bertolami, M. M., & Córscico, A. H. 2013, *A&A*, 557, AA19
- Angulo, C., et al. 1999, *Nuclear Physics A*, 656, 3
- Basu, S., & Antia, H. M. 2008, *Physics Reports*, 457, 217
- Bedin, L. R., Salaris, M., Piotto, G., et al. 2009, *ApJ*, 697, 965
- Bedin, L. R., Salaris, M., King, I. R., et al. 2010, *ApJL*, 708, L32
- Bergeron, P., Saffer, R. A., & Liebert, J. 1992, *ApJ*, 394, 228
- Bono, G., Salaris, M., & Gilmozzi, R. 2013, *A&A*, 549, AA102
- Burgers, J. M. 1969, *Flow Equations for Composite Gases*, New York: Academic Press, 1969
- Carretta, E., Bragaglia, A., Gratton, R., D'Orazi, V., & Lucatello, S. 2009, *A&A*, 508, 695
- Cassisi, S., Potekhin, A.Y., Pietrinferni, A., Catelan, M., & Salaris, M. 2007, *ApJ*, 661, 1094
- Castanheira, B. G., Kepler, S. O. 2009, *MNRAS*, 396, 1709
- Catalán, S., Isern, J., García-Berro, E., et al. 2008a, *A&A*, 477, 213
- Catalán, S., Isern, J., García-Berro, E., & Ribas, I. 2008b, *MNRAS*, 387, 1693
- Caughlan, G. R., Fowler, W. A., Harris, M. J., & Zimmermann, B. A. 1985, *At. Data Nucl. Data Tables*, 32, 197
- Claver, C. F., Liebert, J., Bergeron, P., & Koester, D. 2001, *ApJ*, 563, 987
- Doherty, C. L., Gil-Pons, P., Lau, H. H. B., et al. 2014, *MNRAS*, 441, 582
- Dominguez, I., Chieffi, A., Limongi, M., & Straniero, O. 1999, *ApJ*, 524, 226
- Ferguson, J. W., Alexander, D. R., Allard, F., et al. 2005, *ApJ*, 623, 585
- Freytag, B., Ludwig, H.-G., & Steffen, M. 1996, *A&A*, 313, 497
- García-Berro, E., Hernanz, M., Mochkovitch, R., & Isern, J. 1988a, *A&A*, 193, 141
- García-Berro, E., Hernanz, M., Isern, J., & Mochkovitch, R. 1988b, *NATURE*, 333, 642
- García-Berro, E., Torres, S., Althaus, L. G., et al. 2010, *NATURE*, 465, 194
- García-Berro, E., Torres, S., Althaus, L. G., & Miller Bertolami, M. M. 2014, *A&A*, 571, AA56
- Grevesse, N., & Sauval, A. J. 1998, *Space Science Reviews*, 85, 161
- Groenewegen, M. A. T., & de Jong, T. 1993, *A&A*, 267, 410

- Groenewegen, M. A. T., Sloan, G. C., Soszyński, I., & Petersen, E. A. 2009, *A&A*, 506, 1277
- Haft, M., Raffelt, G., & Weiss, A. 1994, *ApJ*, 425, 222
- Hansen, B. M. S. et al. 2002, *ApJ*, 547, L155
- Hansen, B. M. S., Richer, H. B., Fahlman, G. G., et al. 2004, *ApJS*, 155, 551
- Hansen, B. M. S., Anderson, J., Brewer, J., et al. 2007, *ApJ*, 671, 380
- Hansen, B. M. S., Kalirai, J. S., Anderson, J., et al. 2013, *NATURE*, 500, 51
- Hekker, S., Basu, S., Stello, D., et al. 2011, *A&A*, 530, AA100
- Herwig, F., Blöcker, T., Schönberner, D., & El Eid, M. 1997, *A&A*, 324, L81
- Herwig, F. 2000, *A&A*, 360, 952
- Herwig, F., Freytag, B., Fuchs, T., Hansen, J. P., Hueckstaedt, R. M., Porter, D. H., Timmes, F. X., & Woodward, P. R. 2007, *Why Galaxies Care About AGB Stars: Their Importance as Actors and Probes*, 378, 43
- Horowitz, C.J., Schneider, A.S., & Berry, D.K. 2010, *Physical Review Letters*, 104, 231101
- Hughto, J., Horowitz, C.J., Schneider, A.S., et al. 2012, *Physical Review E*, 86, 066413
- Iben, I., Jr., & MacDonald, J. 1986, *ApJ*, 301, 164
- Iglesias, C.A., & Rogers, F.J. 1996, *ApJ*, 464, 943
- Isern, J., García-Berro, E., Hernanz, M., Mochkovitch, R., & Torres, S. 1998, *ApJ*, 503, 239
- Isern, J., García-Berro, E., & Salaris, M. 2001, *Astrophysical Ages and Times Scales*, 245, 328
- Isern, J., García-Berro, E., Domínguez, I., Salaris, M., & Straniero, O. 2005, 14th European Workshop on White Dwarfs, 334, 43
- Itoh, N., Hayashi, H., Nishikawa, A., & Kohyama, Y. 1996, *ApJS*, 102, 411
- Kalirai, J. S., Richer, H. B., Fahlman, G. G., et al. 2001, *AJ*, 122, 266
- Kalirai, J. S., Richer, H. B., Reitzel, D., et al. 2005, *ApJL*, 618, L123
- Kalirai, J. S., Bergeron, P., Hansen, B. M. S., et al. 2007, *ApJ*, 671, 748
- Kalirai, J. S., Hansen, B. M. S., Kelson, D. D., et al. 2008, *ApJ*, 676, 594
- Kalirai, J. S., Saul Davis, D., Richer, H. B., et al. 2009, *ApJ*, 705, 408
- Kalirai, J. S. 2013, *MmSAI*, 84, 58
- Kalirai, J. S., Marigo, P., & Tremblay, P.-E. 2014, *ApJ*, 782, 17
- Karakas, A., & Lattanzio, J. C. 2007, *PASA*, 24, 103
- Karakas, A. I. 2010, *MNRAS*, 403, 1413
- Kepler, S. O., Pelisoli, I., Koester, D., et al. 2014, arXiv:1411.4149
- Kleinman, S. J., Kepler, S. O., Koester, D., et al. 2013, *ApJS*, 204, 5
- Krauss, L. M., & Chaboyer, B. 2003, *Science*, 299, 65
- Kurtz, D. W., Shibahashi, H., Dhillion, V. S., et al. 2013, *MNRAS*, 432, 1632
- Liebert, J., Bergeron, P., & Holberg, J. B. 2005, *ApJS*, 156, 47
- Lambert, D. L., Gustafsson, B., Eriksson, K., & Hinkle, K. H. 1986, *ApJS*, 62, 373
- Lugaro, M., Herwig, F., Lattanzio, J. C., Gallino, R., & Straniero, O. 2003, *ApJ*, 586, 1305
- Magni, G., & Mazzitelli, I. 1979, *A&A*, 72, 134
- Marigo, P. 2002, *A&A*, 387, 507
- Marigo, P., & Girardi, L. 2007, *A&A*, 469, 239
- Marigo, P., & Aringer, B. 2009, *A&A*, 508, 1539
- Marigo, P., Bressan, A., Nanni, A., Girardi, L., & Pumo, M. L. 2013, *MNRAS*, 434, 488
- Mazzitelli, I., D'Antona, F., & Ventura, P. 1999, *A&A*, 348, 846
- Medin, Z., & Cumming, A. 2010, *Physical Review E*, 81, 036107
- Miglio, A., Brogaard, K., Stello, D., et al. 2012, *MNRAS*, 419, 2077
- Miller Bertolami, M. M., Althaus, L. G., Unglaub, K., & Weiss, A. 2008, *A&A*, 491, 253
- Miller Bertolami, M. M., Althaus, L. G., & García-Berro, E. 2013, *ApJL*, 775, L22
- Moehler, S., Koester, D., Zoccali, M., et al. 2004, *A&A*, 420, 515
- Monelli, M., Corsi, C. E., Castellani, V., et al. 2005, *ApJL*, 621, L117
- Mucciarelli, A., Salaris, M., Lovisi, L., et al. 2011, *MNRAS*, 412, 81
- Ohnaka, K., Tsuji, T., & Aoki, W. 2000, *A&A*, 353, 528
- Paxton, B., Bildsten, L., Dotter, A., et al. 2011, *ApJS*, 192, 3
- Paxton, B., Cantiello, M., Arras, P., et al. 2013, *ApJ*, 208, 4
- Perryman, M. A. C., Brown, A. G. A., Lebreton, Y., et al. 1998, *A&A*, 331, 81
- Prada Moroni, P. G., & Straniero, O. 2002, *ApJ*, 581, 585
- Reimers, D. 1975, *MSRSL*, 8, 369
- Renedo, I., Althaus, L. G., Miller Bertolami, M. M., Romero, A. D., Córscico, A. H., Rohrmann, R. D., & García-Berro, E. 2010, *ApJ*, 717, 183
- Renzini, A., & Fusi Pecci, F. 1988, *ARA&A*, 26, 199
- Renzini, A., Bragaglia, A., Ferraro, F. R., et al. 1996, *ApJL*, 465, L23
- Richer, H. B., Fahlman, G. G., Brewer, J., et al. 2004, *AJ*, 127, 2771
- Richer, H. B., Hansen, B. M., Davis, S., et al. 2006, *Bulletin of the American Astronomical Society*, 38, #228.01
- Rohrmann, R. D., Althaus, L. G., García-Berro, E., Córscico, A. H., & Miller Bertolami, M. M. 2012, *A&A*, 546, A119
- Romero, A. D., Córscico, A. H., Althaus, L. G., et al. 2012, *MNRAS*, 420, 1462
- Romero, A. D., Kepler, S. O., Córscico, A. H., Althaus, L. G., & Fraga, L. 2013, *ApJ*, 779, 58
- Salaris, M., Domínguez, I., García-Berro, E., Hernanz, M., Isern, J., Mochkovitch, R. 1997, *ApJ*, 486, 413
- Salaris, M., Serenelli, A., Weiss, A., & Miller Bertolami, M. 2009, *ApJ*, 692, 1013
- Salaris, M., Althaus, L. G., & García-Berro, E. 2013, *A&A*, 555, AA96
- Schaller, G., Schaerer, D., Meynet, G., & Maeder, A. 1992, *A&AS*, 96, 269
- Schneider, A.S., Hughto, J., Horowitz, C.J., & Berry, D.K. 2012, *Physical Review E*, 85, 066405
- Schröder, K. P., & Cuntz, M. 2005, *ApJL*, 630, L73
- Segretain, L., & Chabrier, G. 1993, *A&A*, 271, L13
- Segretain, L., Chabrier, G., Hernanz, M., et al. 1994, *ApJ*, 434, 641
- Smartt, S. J. 2009, *ARA&A*, 47, 63
- Stancliffe, R. J., Izzard, R. G., & Tout, C. A. 2005, *MNRAS*, 356, L1
- Straniero, O., Domínguez, I., Imbriani, G., & Piersanti, L. 2003, *ApJ*, 583, 878
- Tassoul, M., Fontaine, G., Winget, D. E. 1990, *ApJS*, 72, 335
- Torres, S., García-Berro, E., Burkert, A., & Isern, J. 2002, *MNRAS*, 336, 971
- Tremblay, P.-E., & Bergeron, P. 2008, *ApJ*, 672, 1144
- van Horn, H.M. 1968, *ApJ*, 151, 227
- Vassiliadis, E. & Wood, P. R. 1993, *ApJ*, 413, 641
- Wachlin, F. C., Miller Bertolami, M. M., & Althaus, L. G. 2011, *A&A*, 533, AA139
- Weiss, A., & Ferguson, J. W. 2009, *A&A*, 508, 1343
- Weidemann, V. 1977, *A&A*, 59, 411
- Weidemann, V. 2000, *A&A*, 363, 647
- Winget, D. E., Hansen, C. J., Liebert, J., et al. 1987, *ApJL*, 315, L77
- Winget, D.E., Kepler, S.O., Campos, F., et al. 2009, *ApJL*, 693,

L6

Winget, D. E., Montgomery, M. H., Kepler, S. O., Campos, F.,
& Bergeron, P. 2010, AIPCS, 1273, 146
Wu, Z.-Y., Zhou, X., Ma, J., et al. 2007, AJ, 133, 2061